Griffiths-like phase, large magnetocaloric effect, and unconventional critical behavior in the $NdSrCoFeO_6$ disordered double perovskite

R. S. Silva Jr.,[1,2] C. Santos,[2] M. T. Escote,[3] B. F. O. Costa,[4] N. O. Moreno,[1] S. P. A. Paz,[5] R. S. Angélica,[5] and N. S. Ferreira[1,2,*]

[1]*Department of Physics, Federal University of Sergipe, 49100-000 São Cristóvão, Sergipe, Brazil*
[2]*Laboratory of Corrosion and Nanotechnology (LCNT), Federal University of Sergipe, 49100-000 São Cristóvão, Sergipe, Brazil*
[3]*Center for Engineering, Modeling, and Applied Social Sciences, Federal University of ABC, 09210-580 Santo André, São Paulo, Brazil*
[4]*University of Coimbra, CFisUC, Department of Physics, P-3004-516 Coimbra, Portugal*
[5]*Institute of Geosciences, Federal University of Pará, 66075-110 Belém, Pará, Brazil*

(Received 16 April 2022; revised 2 October 2022; accepted 3 October 2022; published 31 October 2022)

A B-site disordered double perovskite $NdSrCoFeO_6$ was successfully synthesized by the conventional sol-gel method. Detailed experimental analyses revealed that $NdSrCoFeO_6$ crystallizes in the orthorhombic *Pnma* space group, in which $Co^{2+/3+}$ and $Fe^{3+/4+}$ ions are randomly distributed at the BB′ sites, and Sr^{2+} and Nd^{3+} ions are respectively ordered at the A and A′ sites in an alternating arrangement along the c direction. $NdSrCoFeO_6$ has a semimetallic-to-semiconducting transition nature, and a paramagnetic-ferromagnetic (FM) second-order phase transition originating from the complex hybridization between Co $3d$ and O $2p$ states is also found to occur at $T_C \approx 150$ K. Then the spin coupling between $Fe^{4+} \leftrightarrow Co^{3+}$ and $Fe^{3+} \leftrightarrow Co^{2+}$ randomly distributed on the B and B′ sites leads to a FM cluster spin-glass behavior with characteristic parameters of $k = 0.01$, $T_{SG} = 82.7$ K, $zv = 1.89$, and $\tau_0 = 0.46 \times 10^{-4}$ s. Additionally, Griffiths-like phase behavior was observed in the region $T_C < T < T_{GP}$, with $T_{GP} = 245$ K, consistent with the power law exponent of $\lambda = 0.74$. The maximum isothermal magnetic entropy change $-\Delta S_M^{max} \approx 1.84\,J\,kg^{-1}\,K^{-1}$ and relative cooling power $\approx 43.8\,J\,kg^{-1}$ under a field of 40 kOe also indicate a magnetocaloric coupling wherein fitted critical exponents $\beta = 1.384$, $\gamma = 0.621$, and $\delta = 1.421$ are far from any conventional universality class. Density functional theory calculations demonstrated spin short- and long-range ordering competitions for Fe/Co at BB′ sites, which arise predominantly from the stronger negatively charged ligand interaction with Co $3d$ orbitals and the weakest Fe $3d$ orbitals. This unconventional behavior is expected to be the main reason for the experimentally observed magnetic exchange distance decreasing with $J(r) \approx r^{-4.7}$.

DOI: 10.1103/PhysRevB.106.134439

I. INTRODUCTION

The fascinating flexibility of $AA'BB'O_6$-type double perovskites (DPs) lies in the possibility of combining several ions in their structure, both with elements at the A/A′ site [rare earths (REs)] and at the B/B′ site [transition metals (TMs)], or simultaneously, which can result in a diverse range of interesting and potentially useful physical properties, such as catalytic activity, electronic and ionic conductivity, chemical stability, and magnetic ordering [1,2]. Usually, when the different combinations are at the B/B′ site (with different ionic radii), different exchange interactions are observed, playing important roles in increasing oxygen defects and improving oxygen transport. Thus, the charge ordering of the elements introduced by the B-O-B′ combinations can give rise to interesting semiconductor, dielectric, ferroelectric, and thermomagnetic properties [3]. Recently, the Co/Fe-based DPs (B/B′ site) have drawn much attention due to their diverse application possibilities, such as cathode material for intermediate temperature solid oxide fuel cells [4], magnetic catalysts [5], thermoelectric materials [6], nonvolatile memories [7], spintronics [8], and magnetic refrigeration [9]. Most of these DPs containing Co and/or Fe in their lattices crystallize in a monoclinic structure with $P2_1/n$ space group setting the ordered state or in an orthorhombic structure with $Pbnm/Pnma$ space group setting a disordered state [10–14]. In this context, various properties can be observed due to the flexibility in designing the interplay of charge, spin, and phonons, which comes from different arrangements of the ions in the structure. For instance, the ordered state favors the appearance of the magnetic interactions between Co^{2+}/Fe^{2+}, Co^{3+}/Fe^{3+}, and Co^{4+}/Fe^{4+} ions, while the disordered state induces additional interactions of the Co^{2+}/Fe^{2+}-O^{2-}-Co^{2+}/Fe^{2+}, Co^{3+}/Fe^{3+}-O^{2-}-Co^{3+}/Fe^{3+}, or Co^{4+}/Fe^{4+}-O^{2-}-Co^{4+}/Fe^{4+} types [15,16]. However, the origin of the magnetic and electronic interactions is still unclear because of the lack of systematic studies on the fundamental properties of these materials, encouraging us to understand how local interactions can influence their properties.

Interestingly, the coexistence of various magnetic interactions such as Co^{2+}/Fe^{2+}-O^{2-}-Co^{2+}/Fe^{2+}, Co^{2+}/Fe^{3+}-O^{2-}-Co^{3+}/Fe^{2+}, Co^{3+}/Fe^{3+}-O^{2-}-Co^{3+}/Fe^{3+}, Co^{2+}/Fe^{4+}-O^{2-}-Co^{4+}/Fe^{4+}, Co^{4+}/Fe^{4+}-O^{2-}-Co^{4+}/Fe^{4+},

*nilson@academico.ufs.br

and Co^{3+}/Fe^{4+}-O^{2-}-Co^{4+}/Fe^{3+} in these DP structures leads to the observation of the ferromagnetic (FM) double-exchange interactions that coexist and compete with the antiferromagnetic (AFM) superexchange interactions, which result in fascinating magnetic properties. For instance, de Oliveira *et al.* [13] observed for the Nd_2CoFeO_6 sample that the high degree of antisite disorder (ASD) reduces the effective magnetic moment (μ_{eff}) in the structure for the Co^{3+} ions being in a low spin state and the FM component coming from a coupling of Fe^{3+} clusters. According to Mazumdar and Das [16], octahedral distortion with the bond angle diverging from 180° induces imperfect superexchange interactions in these structures, known as a Dzyaloshinskii-Moriya (DM) antisymmetric exchange interaction. This leads to a canted AFM state below the magnetic transition temperature, causing weak ferromagnetism (WFM) due to the small canting of the spins from the AFM crystallographic axis. Recently, Sahoo *et al.* [11] analyzed $LaSrCoFeO_6$ crystals by x-ray photoelectron spectroscopy (XPS) and demonstrated that the Co and Fe ions assume 3+ and 4+ valences. Then by considering the spin-only moment, their observation pointed to a significant exchange bias (EB) effect ($H_{\text{EB}} \approx 1.2$ kOe) and spin-glass (SG) states, originated due to local magnetic frustration at low temperatures by ASD. Moreover, previous reports show that compounds containing Fe and Co ions in the B/B′ site can possess complex valence states and that Fe-O-Co superexchange interactions can favor electronic transfer from the Fe^{3+} ($t_{2g}^3 e_g^2$) high-spin (HS) state to the Co^{4+} ($t_{2g}^5 e_g^0$) low-spin (LS) state [17–19]. Furthermore, the Griffiths-like phase (GP) existence is very often reported in DP FMs [10,20–22]. According to Pal *et al.* [10], the presence of the GP can occur from disorders associated with the random distribution of Co and Fe ions at site $4b(0.5; 0; 0)$ in the crystal structure. Moreover, competitions between AFM and FM interactions promoted by the spin cant create random exchange interactions, which can also originate from a GP. However, Silva *et al.* [20] suggest that this appearance of the GP is quite likely caused by the magnetic dilution inherent to nonmagnetic Co^{3+} ($t_{2g}^6 e_g^0$) in the LS state, which makes it difficult to induce a long-range order. On the other hand, the GP observed by Nasir *et al.* [21] in La_2FeMnO_6, with orthorhombic crystal structure (*Pbnm*), arises due to the short-range ferrimagnetic ordering in a paramagnetic (PM) matrix and is highly sensitive to changes in the applied magnetic field. Curiously, Das *et al.* [15] demonstrated that the evolution of the inverse susceptibility as a function of temperature and external field for Gd_2CoMnO_6 with a monoclinic unit cell ($P2_1/n$) is not consistent with the GP. This was consistently confirmed by a detailed analysis of the critical behavior, whereas the observed values of critical exponents $\beta = 1.18$, $\gamma = 0.65$, and $\delta = 1.55$ associated with the FM-to-PM phase transition are far from any known existing universality class. Further, reports correlating GP with critical exponents are lacking.

The exchange interactions between $3d$ (Co/Fe) and $4f$ (RE) orbitals are also observed in these DP structures and can induce an interesting magnetocaloric effect (MCE) as those observed for Gd_2FeCoO_6 ($-\Delta S_M^{\max} = 7.82\,\text{J kg}^{-1}\,\text{K}^{-1}$) and Er_2FeCoO_6 ($-\Delta S_M^{\max} = 8.85\,\text{J kg}^{-1}\,\text{K}^{-1}$) [23]. These results are quite relevant when compared with those recently published for the FM alloy $PrCrGe_3$ ($-\Delta S_M^{\max} \sim 3.2\,\text{J kg}^{-1}\,\text{K}^{-1}$) and freestanding gadolinium thick films ($-\Delta S_M^{\max} \sim 8.3\,\text{J kg}^{-1}\,\text{K}^{-1}$) at 5 T field [24,25]. However, these values are still far from some Gd-based reference materials such as $Gd_3Ga_5O_{12}$ ($-\Delta S_M^{\max} \sim 32\,\text{J kg}^{-1}\,\text{K}^{-1}$) and $GdVO_4$ ($-\Delta S_M^{\max} \sim 41\,\text{J kg}^{-1}\,\text{K}^{-1}$) [26,27], which have the Heisenberg characteristic to fully align the Gd ions faster, thus producing a significant change in magnetic entropy. Differently, Sahoo *et al.* [28] reported that the spin orderings and orbital related to the MCE could be tuned by doping with divalent alkaline-earth metals (Sr, Ca, etc.) at the RE site (Gd, Nd, etc.) in DP structures. Surprisingly, their results showed that Sr substitution of Gd ions of ∼25% in Gd_2CoMnO_6 significantly suppresses the independent spin order, leading to enhancement of ferromagnetism, contributing to a giant MCE of $-\Delta S_M^{\max} \sim 21\,\text{J kg}^{-1}\,\text{K}^{-1}$ at low temperature. They also concluded that the enhanced FM and large value of $-\Delta S_M^{\max}$ are a result of the less independent Gd spin ordering (Gd^{3+}-Gd^{3+}) and canting of the antiparallel spins of Gd. However, Krishna Murthy *et al.* [29] reported that the MCE is clearly suppressed by $3d$-$4f$ interactions in $Gd_2(TM)MnO_6$ from ∼35 to ∼24 $\text{J kg}^{-1}\,\text{K}^{-1}$ when the TM changes from Ni to Co. Thus, this scenario highlights the unflagging search for RE systems with better magnetocaloric performances for practical technology and encourages exploration of the underlying physics of the MCE.

In this paper, we report the structural, electronic, and magnetic study of the disordered DP $NdSrCoFeO_6$ using a combination of x-ray diffraction (XRD) and Rietveld refinement analysis, dc and ac magnetization measurements, ^{57}Fe-Mössbauer spectroscopy, magnetocaloric properties analysis, and density functional theory (DFT) calculations. The structural results demonstrate that $NdSrCoFeO_6$ crystallizes into a distorted orthorhombic structure with the *Pnma* space group. Magnetic measurements, XPS, and ^{57}Fe-Mössbauer spectroscopy results reveal that the multiple magnetic transitions observed are associated with Fe^{4+} and Fe^{3+}/Co^{2+} in an LS/HS state, while Co^{3+} in the possible HS and intermediate-spin state, as well as apparent GP behavior, was observed. Moreover, critical exponents β, γ, and δ, obtained through the scaling analysis of magnetization data, and the magnetocaloric results demonstrate distance from any conventional universality class. The magnetic exchange distance decreases with $J(r) \approx r^{-4.7}$ between the three-dimensional (3D) Heisenberg and mean-field model; the competition between long- and short-range magnetic interaction should be responsible for critical behavior in $NdSrCoFeO_6$.

II. EXPERIMENTAL DETAILS

A. Synthesis

The $NdSrCoFeO_6$ DP was synthesized by the conventional sol-gel method. Appropriate amounts of $Nd(NO_3)_3 \cdot 6H_2O$, $Sr(NO_3)_2$, $Co(NO_3)_3 \cdot 6H_2O$, and $Fe(NO_3)_3 \cdot 9H_2O$ with a 1:1:1:1 (Nd : Sr : Co : Fe) ratio were dissolved in 5 mL of distilled water, followed by the addition of the glycine

($C_2H_5NO_2$) as a chelating agent. Then the homogenized solution was dried at 100° C for 24 h for gelification and dehydration. Afterward, the obtained xerogel was calcined at different temperatures of 800° C (2 h), 1000° C (4 h), and 1200° C (6 h).

B. Characterization

XRD analysis was carried out in a divergent beam diffractometer (Empyrean, PANalytical) equipped with $\theta-\theta$ goniometer, the Co-sealed x-ray tube ($K_{\alpha 1} = 1.78901$ Å), $k\beta$ iron metallic filter, and a PIXel^{3D} 2×2 area detector with an active length of 3.3473° 2θ (255 active channels). Instrument conditions were as follows: 20°–90° (2θ) range; 40 kV and 40 mA; 0.01° 2θ step size and 20 s time per step; 1/2° divergent slit and 1° antiscattering; 10-mm irradiated sample size; and sample spinning with 2 rotations per second. The instrument resolution was assessed using the LaB_6 NIST/SRM 660b standard. Rietveld refinements were performed using FULLPROF software [30]. The microstructural and structural details of the sample were examined by selected area electron diffraction (SAED) pattern and high-resolution transmission electron microscopy (HRTEM) using a Tecnai G2 F20 S-TWIN transmission electron microscope (TEM) at the accelerating voltage of 200 kV. The Miller index identification on SAED patterns was made with CRYSTBOX software using ring analysis mode (ring GUI) [31]. Image processing was performed with Digital Micrograph Software (Gatan, Inc.). The ^{57}Fe-Mössbauer spectrum was taken at 300 K in transmission geometry using a 50 mCi ^{57}Co(Rh) γ-ray source. The velocity scale of the spectra was calibrated relative to α-Fe foil. Data processing was done using WINNORMOS [32]. Core-level XPS was performed using a ThermoFisher Scientific K-Alpha$^+$ spectrometer equipped with a monochromatic Al-Kα x-ray source ($h\nu = 1.486.6$ eV) operating at 100 W. Samples were analyzed under vacuum ($p < 10^{-8}$ mbar) with a pass energy of 25 eV. The binding energy scale of the spectra was adjusted to the binding energy of the adventitious carbon C-(C,H) at 284.8 eV. Peak areas were obtained from fitting the spectra and relative sensitivity factors from the atomic photoionization cross-section of each core level provided by the SPECS Prodigy library. The dc magnetization measurements of the sample were performed using a Magnetic Properties Measurement System with a 7 T magnet equipped with a vibrating sample magnetometer (VSM) option (MPMS3, Quantum Design, USA). Temperature-dependent magnetization $M(T)$ was measured under zero-field-cooled (ZFC) and field-cooled (FC) procedures. Furthermore, the temperature variation of ac susceptibility $\chi_{ac}(T)$ at different frequencies ranging from 10 to 1000 Hz was measured with an ac susceptometer attached to the Physical Property Measurement System (PPMS, Quantum Design, USA). The electrical resistivity (ρ) was also measured in the PPMS at magnetic fields of 0 and 100 Oe in the temperature range from 150 to 300 K. The isothermal $M(H)$ curves were measured, ranging the magnetic field from 0 to ±40 kOe. The MCE was estimated from the magnetization measurements vs the applied magnetic field at several temperatures with $\Delta T = 2$ K.

C. Computation methods

The magnetic behavior and electronic structure of $NdSrCoFeO_6$ were studied by first-principles calculations based on DFT [33,34] using the full-potential linearized-augmented-plane-wave method [35] implemented in the WIEN2K program [36]. During the calculations, the radii R_{Mt} of the nonoverlapping muffin-tin sphere were chosen as 2.36, 2.15, 1.85, 1.90, and 1.56 a.u. for Nd, Sr, Co, Fe, and O, respectively. The atomiclike functions inside the sphere were developed up to $l_{max} = 10$, and in the interstitial region, a plane-wave expansion was limited at $k_{max} = 7.0/R_{MT}(O)$. The charge density was Fourier expanded with $G_{max} = 14$, and the valence electronic states of O ($2s^2\,2p^4$), Fe ($3d^6\,4s^2$), Co ($3d^7\,4s^2$), and Nd ($5s^2\,5p^6\,4f^3\,6s^2$) were considered explicitly in the calculations. For the k-space integration, we employed a proper k-mesh using $5 \times 6 \times 5$ k-points in the irreducible part of the Brillouin zone (IBZ). In all calculations, applying PBEsol generalized gradient approximation functional [37] combined with the onsite Coulomb correction (PBE + U) considered exchange-correlation effects between electrons. The Hubbard U term is based on the Anisimov *et al.* [38] method using the effective $U_{eff} = U\text{-}J$ potential. We used 3.0 eV to describe the Nd f orbitals and 4.0 eV for the d states of Co and Fe ions. Tests varying U_{eff} potential from 1 to 7 eV applied on localized Nd f states showed no significant change of its magnetic moment relative to the 3.0 eV considered value. For self-consistent calculations, we selected a good level of convergence, and all systems have been successfully converged in energy (10^{-5} Ry) and charge (10^{-5} eV/bohr^3 transfer criteria. The relaxation of internal parameters was conduced until the forces between atoms were reduced by <2 mRy/bohr.

III. RESULTS AND DISCUSSION

A. Crystalline structure

The crystal structure and phase purity of the $NdSrCoFeO_6$ DP were studied by XRD. The XRD patterns of the $NdSrCoFeO_6$ sample calcined at 800, 1000, and 1200° C presented diffraction peaks corresponding to the crystallographic planes (101), (020), (200), (121), (220), (022), (202), (040), (301), (222), (103), (321), (123), (400), (242), and (004), characteristic of the orthorhombic-type structure with space group *Pnma* (62) (ICSD #153437), as shown in Fig. 1(a). However, small peaks associated with minor secondary phases are observed in the XRD pattern of the samples calcined at 800 and 1000° C. The diffraction peaks at $2\theta = 42.74°$ and 52.31° are identified as the Co_3O_4 phase (ICSD #69367), and the diffraction peaks at $2\theta = 29.98°$, 37.24°, 42.86°, 49.57°, 57.05°, 77.11°, and 79.43° correspond to the $Sr_8Co_4Fe_4O_{23}$ phase (ICSD #246261). No impurity peak is observed for the $NdSrCoFeO_6$ sample calcined at 1200° C within the resolution limit of the instrument, suggesting a highly pure and single-phase material. This result agrees with those previously reported for $SmSrCo_2O_{5+\delta}$ and $GdSrCo_2O_{5+\delta}$ DPs [39,40]. A typical Rietveld XRD pattern is shown in Fig. 1(b) for the $NdSrCoFeO_6$ sample, and the obtained Rietveld parameters are summarized in Table I. The reliability factors $R_p = 5.56\%$, $R_{wp} = 7.05\%$, $R_{exp} = 6.19\%$, and $\chi^2 = 1.35$

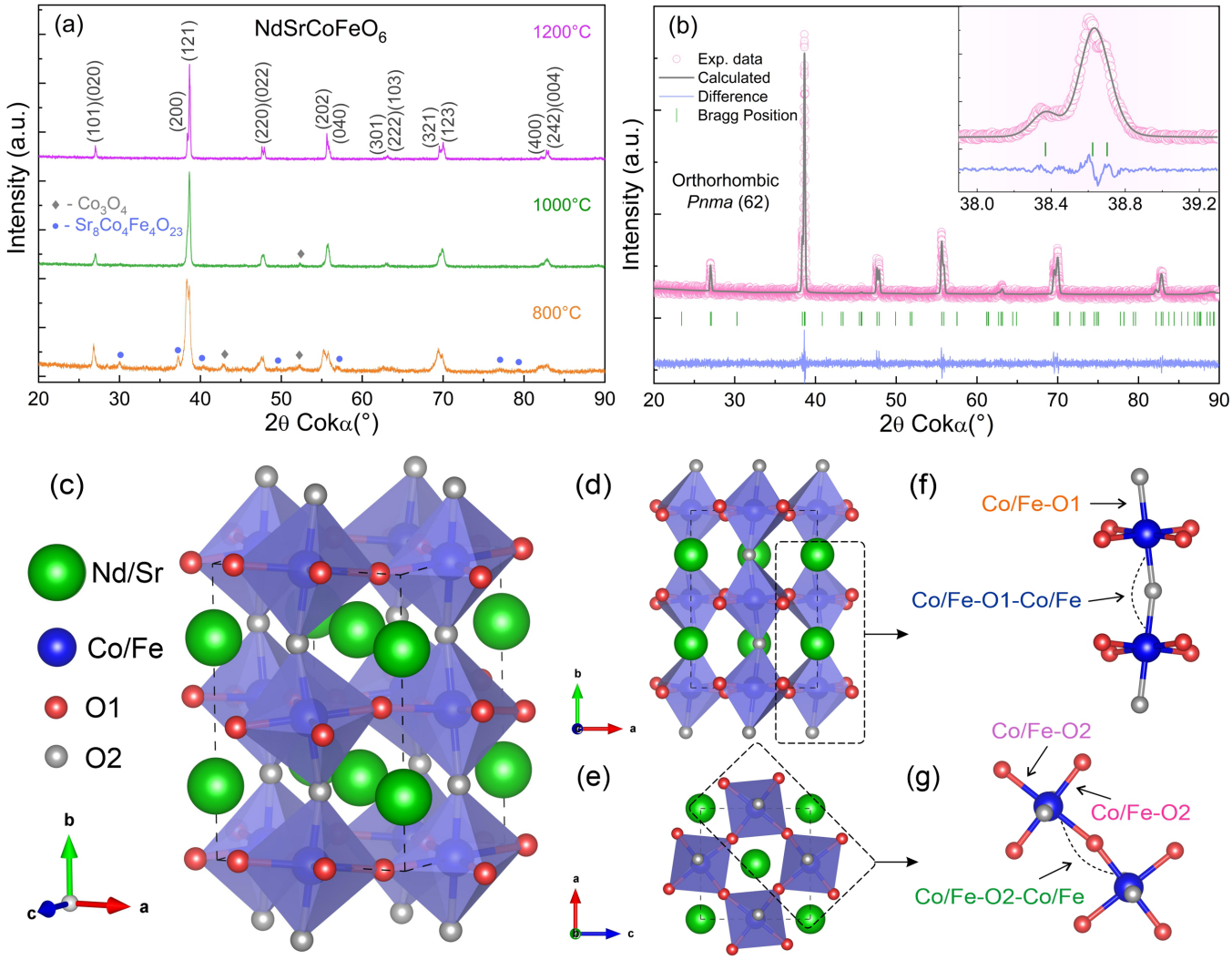

FIG. 1. (a) X-ray diffraction (XRD) patterns for $NdSrCoFeO_6$ sample calcined in different temperatures (800, 1000, and 1200° C), and (b) Rietveld refinement for sample calcined at 1200° C. (c)–(g) Detailed local crystalline structure for the $NdSrCoFeO_6$ sample and their corresponding interatomic distance variations and bond angle distortions. The big green balls and red/gray small balls represent Nd/Sr and O atoms, respectively, while blue octahedra denote $(Co/Fe)O_6$.

TABLE I. Results of Rietveld refinement for the $NdSrCoFeO_6$ DP.

Parameters	$NdSrCoFeO_6$
Space group	*Pnma*
Lattice parameters	$a = 5.44672(3)$ Å
	$b = 7.63664(2)$ Å
	$c = 5.40311(6)$ Å
	$V = 224.74(1)$ Å^3
Refinement parameters	$R_p = 5.56\%$
	$R_{wp} = 7.05\%$
	$R_{\text{exp}} = 6.19\%$
	$\chi^2 = 1.35$
Bond lengths (Å)	Co/Fe-O1 = 1.926(7)
	Co/Fe-O2 = 1.89(4)
	Co/Fe-O2 = 1.99(5)
	⟨Co/Fe-O⟩ = 1.938(6)
Bond angles (Å)	Co/Fe-O1-Co/Fe = 164(3)
	Co/Fe-O2-Co/Fe = 162(3)
	⟨Co/Fe-O-Co/Fe⟩ = 163(3)

indicate good agreement between the refined and experimental XRD patterns, confirming the orthorhombic phase present in this material with lattice parameters $a = 5.44672(3)$ Å, $b = 7.63664(2)$ Å, $c = 5.40311(6)$ Å, and unit-cell volume $V = 224.74(1)$ Å^3. Figures 1(c)–1(g) exhibit the detailed local crystalline structure generated with VESTA software [41] and their corresponding interatomic distance variations and bond angle distortions, where Co/Fe are octahedrally coordinated with six oxygen atoms. From the value of the Goldschmidt tolerance factor (t_G) [42], it is possible to predict the structural stability along with the tendency of structural deformation of the structure, in our case, given by $t_G = \frac{(\frac{r_{Nd} + r_{Sr}}{2}) + r_O}{\sqrt{2}\,(\frac{r_{Co} + r_{Fe}}{2} + r_O)}$, where r is the ionic radii elements [43]. The calculated values of t_G for the $NdSrCoFeO_6$ DP are 0.938 and 0.901 for the LS and HS states of Co^{3+} and Fe^{3+} (VI coordination number), respectively, which is expected for an orthorhombic structure [44].

In this type of orthorhombic crystal structure, both Nd/Sr cations and O_1^{2-} anions occupy the $4c(x, \frac{1}{2}, z)$ sites, and B-site

cations like Co/Fe are aleatorily distributed at the $4b(\frac{1}{2}, 0, 0)$ sites. The $8d(x, y, z)$ position is generally occupied by O_2^{2-} anions [16]. Owing to the random distribution of the Co and Fe ions (B/B′ site) in the same atomic position, the structure becomes centrosymmetric, as reported by Anderson *et al.* [45], in the case of the Co/Fe sublattices being predominantly in the same 3+ valence state.

The local crystal structure [Figs. 1(c)–1(g)] indicates that the bond length and bond angle are not particularly identical, i.e., Co/Fe-O1 ≠ Co/Fe-O2 and Co/Fe-O1-Fe/Co ≠ Co/Fe-O2-Fe/Co ≠ 180°, as shown in Table I. This indicates the presence of a distorted crystalline structure in the $NdSrCoFeO_6$ system. The average bond length ⟨Co/Fe-O⟩ = 1.938(6) Å and average bond angle ⟨Co/Fe-O-Co/Fe⟩ = 163(3) Å obtained from the structural refinement are in agreement with those obtained for other DPs with orthorhombic structure [10,14,16,21,46]. Herein, the bond length (Co/Fe-O) and bond angle (Co/Fe-O-Co/Fe) are different from those found for an ordered DP compound at room temperature [47]. However, the calculated octahedral distortion by considering the average bond angle using the formula $\Phi = [180 - \langle$Co/Fe-O-Co/Fe$\rangle]/2$ [16] is $\Phi = 8.4°$, indicating that the octahedra are slightly distorted from their equilibrium position, in agreement to other DPs previously reported [14,48]. Generally, the disorder and this kind of distorted crystal structure in most of the perovskites influence the magnetic competition and frustration effects in these materials [11]. In our disordered $NdSrCoFeO_6$ system, a similar scenario could also be expected.

The crystal structure of the $NdSrCoFeO_6$ sample was further confirmed by TEM characterization. Figure 2(a) shows a low-magnification TEM image of the sample, whereas dense secondary particles with an average size of ∼470 nm are noticed. We further applied HRTEM measurements to the sample [see Fig. 2(b)], where it was demonstrated that these secondary particles are composed of aggregated smaller primary nanosized particles with an average size in the range of ∼7–10 nm. Moreover, the lattice parameters were measured from the HRTEM images and the positions of the concentric diffraction rings in the SAED patterns [Figs. 2(b) and 2(c)]. HRTEM shows clear lattice fringes with d spacing of ∼0.28 and ∼0.47 nm, corresponding to (200) and (001) planes. The SAED patterns taken from the area presented in the TEM images in Fig. 2(b) show clearly distinct rings ascribed to (002), (040), (232), (261), and (026) planes. This SEAD investigation confirmed the formation of highly polycrystalline $NdSrCoFeO_6$, posing an orthorhombic crystal structure with space group *Pnma* (ICSD #153437) in good agreement with the XRD Rietveld refinement studies. Using these parameters, we have projected a model of the crystal structure of $NdSrCoFeO_6$ in VESTA software [41], which is set on the upper right side of the enlarged HRTEM image shown in Fig. 2(d). It can be observed that a probable atomic arrangement of Na/Sr, Co/Fe, and O atoms in $NdSrCoFeO_6$ is based on both XRD and HRTEM data. The ordered arrangement in $NdSrCoFeO_6$ ($AA'BB'O_{6+\delta}$) points to a lower-valence A′ (Sr) cation substituting an A (Nd)-site cation, which results in a layered structure, whereas the A and A′ cations show an alternating arrangement along the c direction. Moreover, the

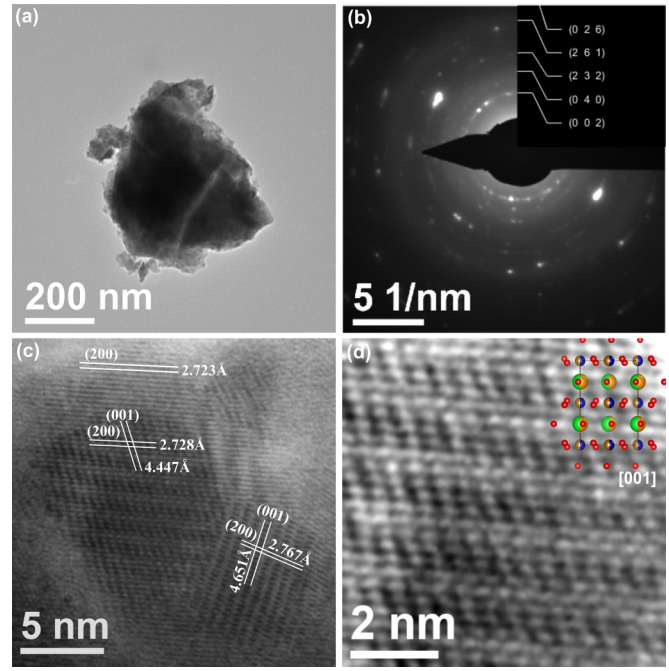

FIG. 2. (a) Typical transmission electron microscope (TEM) image along with the (b) corresponding selected area electron diffraction (SAED) pattern. (c) High-resolution TEM (HRTEM) image showing lattice fringes of the $NdSrCoFeO_6$ sample. (d) Magnified HRTEM micrographs along the [001] direction. The inset shows a schematic crystal structure of $NdSrCoFeO_6$. Green/golden, blue/yellow, and red dots represent Nd/Sr, Co/Fe, and O atoms.

double oxygen atomic columns are mainly oriented along the y and z directions in a zigzag fashion. This zigzag orientation feature suggests that the accommodation of Sr^{2+} ions in the octahedral structure results in stronger octahedral tilting. Meanwhile, the random distribution of the Co^{3+}/Co^{4+} ions is slightly smaller than Fe^{3+}/Fe^{4+} ions (B/B′ site) in the same atomic position. This induces the formation of long-range ordered defect structures due to located oxygen vacancies ($\delta < 1$) at the AO_δ layers in which the electroneutrality of the $NdSrCoFeO_6$ structure is reached by the higher mobility of the oxygen ions [49,50].

B. Magnetism

The ion disorder of the $NdSrCoFeO_6$ DP can lead to the coexistence of multiple magnetic interactions, resulting in fascinating magnetic properties. Firstly, to investigate the magnetic phase transition temperature and reveal the intrinsic magnetic interactions in the $NdSrCoFeO_6$ sample, the magnetization dependence with the temperature (M-T) was measured in the temperature range of 2–300 K under various applied magnetic fields (H_{dc}). Figure 3(a) shows the M-T curve measured at $H_{dc} = 10$ Oe under ZFC and FC conditions. The result indicates a typical FM behavior at low temperature and a sharp transition to a PM state. Similar behavior in the M-T curve has also been observed in other DP systems [12,17,20,51]. The nonlinear response observed < ∼20 K is understood as a combination of the canted AFM order of the Co^{3+}/Fe^{3+} sublattice combined with the Nd^{3+} PM behavior,

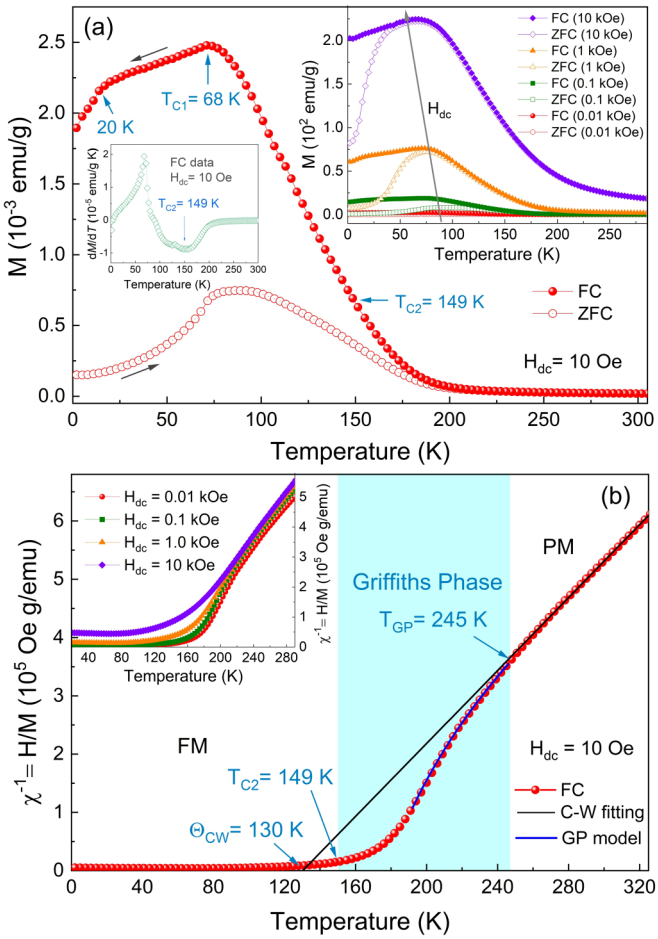

FIG. 3. (a) Magnetization dependence with the temperature (M-T) of $NdSrCoFeO_6$ sample measured at $H_{dc} = 10$ Oe under zero-field-cooled (ZFC) and field-cooled (FC) conditions. The right inset shows the minimum derivative $dM/dT(T)$ associated with T_{C2}, and the left inset shows M-T curves (ZFC/FC) for different H_{dc}, where the arrow indicates the direction of increase of the field. (b) The inverse susceptibility ($\chi^{-1} = H/M$) as a function of temperature measured at $H_{dc} = 10$ Oe. The black line shows the linear fit to the Curie-Weiss (CW) law. The blue highlight shows the existence of the Griffith phase with $T_{GP} = 245$ K. The blue line is the best fit of the GP model of Eq. (1) to the $\chi^{-1}(T)$ data with parameters $T_C^R = 149$ K and $\lambda = 0.74$. The inset shows $\chi^{-1}(T)$ curves for different H_{dc} (0.01 to 10 kOe).

as observed in several compounds containing Nd-Fe interactions [13,15,52]. Furthermore, sharing nonmagnetic Sr^{2+} ions at the Nd^{3+} site favor a disordered crystal structure and with the oxygen vacancy, making the system frustrated, which can lead to Nd^{3+}-O^{2-}-Nd^{3+} ($4f$-$4f$) weak short-range interaction at low temperature [28].

The transition temperatures were estimated from the first derivative of M_{FC} (dM_{FC}/dT) [shown in the right-side inset of Fig. 3(a)]. The dM_{FC}/dT vs T curve suggests that there are two ordering temperatures $T_{C1} = 68$ K and $T_{C2} = 149$ K [highlighted in Fig. 3(a)]. The first transition at 68 K (lock temperature), determined by the maximum in $dM_{FC}/dT(T)$, suggests a domain dynamic originating from mixed FM and AFM regions existing in the $NdSrCoFeO_6$ sample due to ASD [11,53]. Moreover, the presence of octahedral distortion through the Co/Fe-O-Co/Fe bond angle diverging from 180° (observed in Table I) has also been reported to induce imperfect superexchange interaction, which is a DM antisymmetric exchange interaction, resulting in canted AFM states below the magnetic transition temperature [16]. Additionally, we can see a spontaneous FM ordering smeared throughout ~68 K up to the second transition temperature $T_{C2} = 149$ K in the $dM_{FC}/dT(T)$ curve, which was determined as the minimum temperature. Above this temperature, the magnetic ordering changes to the PM state, where magnetic moments become disordered under the impact of thermal energy.

Furthermore, strong magnetic irreversibility <149 K is clearly visible in the ZFC and FC curve measured under a field of 10 Oe. With the increase of the applied field ($H_{dc} =$ 0.01–10 kOe) is observed a sharp increase at low temperature for the magnetization, the ZFC/FC curves tend to merge, and the FC arm shows signs of saturation with a broadening of the peak [see inset in Fig. 3(a)]. This confirms the presence of a majority FM phase since, for an AFM, the increase in the field would have little effect on the magnetization [15]. Moreover, it is seen that the irreversibility temperature (T_{irr}) is shifted toward the low-temperature regime with the increase of H_{dc} (0.01 up to 10 kOe). This behavior is also observed for other DPs [51,54–56]. According to Sahoo *et al.* [11], this shift can be assigned to a SG or superparamagnetic (SPM) behavior. Moreover, the competing FM and AFM interactions result in local magnetic frustration at low temperatures due to the ASD, resulting in an SG behavior [1]. Usually, for most of the canonical SG systems, the onset of the irreversibility point is very close to the glassy temperature [11,57,58]; however, in our system, the onset of the irreversibility point is reasonably above this temperature, at $T_{irr} \sim 200$ K (for $H_{dc} = 10$ Oe), resembling cluster-glass (CG) states. This type of behavior has already been reported in various systems of DPs such as $La_{2-x}Sr_xCoMnO_6$ [59], $La_{1.5}Ca_{0.5}CoMnO_6$ [57], Pr_2CoFeO_6 [10], $SrLaFeCoO_6$ [53], and $La_{1.8}Pr_{0.2}CoFeO_6$ [7]. Thus, the SG-like frozen magnetic state most likely exists in our $NdSrCoFeO_6$ sample in a low-temperature regime.

To investigate further into the SG behavior as well as dynamics of SG in the $NdSrCoFeO_6$ sample, real (χ'_{ac}) and imaginary (χ''_{ac}) parts of magnetic ac susceptibility measurements have been carried out in the temperature range of 5–220 K, with an ac field of $H_{ac} = 0.4$ Oe and different frequencies (10–1000 Hz), as shown in Figs. 4(a) and 4(b). Both $\chi'_{ac}(T)$ and $\chi''_{ac}(T)$ parts show a low-intensity broad shoulder ~150 K (at the beginning of the magnetic ordering). However, it has no frequency dependence, which does not characterize the signature of SG behavior. Therefore, it can be inferred that the transition ~150 K is of the FM type [60]. By further decreasing the temperature, a maximum peak is observed in both parts between 70 and 85 K. Clearly, the frequency dependency in $\chi'_{ac}(T)$ is shifted toward higher temperature, and the magnitude decreases, while in $\chi''_{ac}(T)$, the magnitude increases, this behavior being quite like that observed in other FM materials, which can be associated with SG or SPM behavior [61–63]. To further clarify, the relative shift (k) in freezing temperature can be used to describe the magnetic order of the system, which is denoted as $k = \frac{\Delta T_f}{T_f[\Delta \log(\omega)]}$ [57], where ΔT_f is the maximum change in the freezing temperature (here,

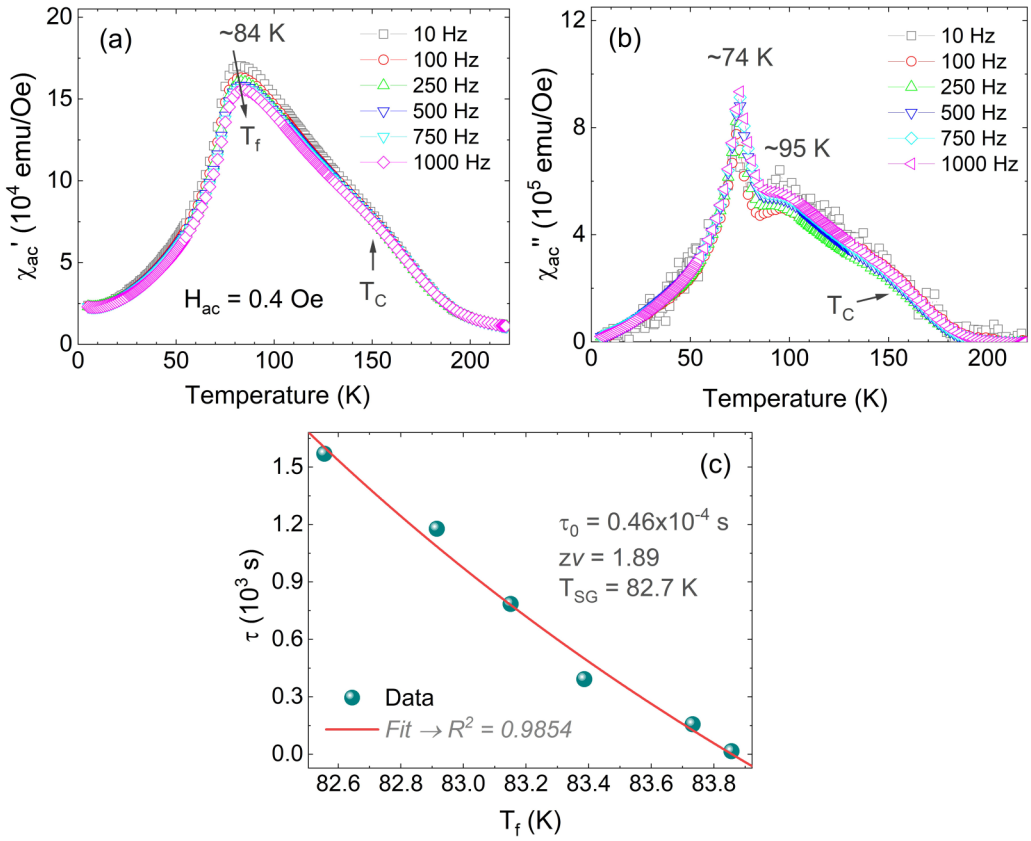

FIG. 4. Temperature dependence of (a) real χ'_{ac} and (b) imaginary χ''_{ac} parts of the ac magnetic susceptibility measured at fixed different frequencies (10 to 1000 Hz) for $NdSrCoFeO_6$ sample. (c) The best fit to power law of τ vs T_f plot.

$\Delta T_f = 1.9$ K). Typically, this value lies between 0.005 and 0.08 for a SG and is >0.2 for noninteracting SPM materials [57,61]. The obtained value of 0.01 confirms our system to be more likely an SG type with a freezing temperature $T_f \sim$ 84 K. Generally, in the SG system, the relaxation time (τ) around transition temperature is described by the power law:

$$\tau = \tau_0 \left[\frac{T_f}{T_{SG}} - 1 \right]^{-zv}, \quad T_f > T_{SG}, \tag{1}$$

where T_{SG} is the freezing temperature as the frequency tends to zero, τ_0 is the characteristic flipping time of a single spin flip, $\tau = 1/2\pi f$ is the relaxation time, zv is the dynamical critical exponent, and T_f is the frequency dependence of the peak position in $\chi'_{ac}(T)$ [64]. The τ vs T_f plot along with the fit to the critical power law is shown in Fig. 4(c). Usually, in a conventional SG system, the typical value for zv is in the range of 4–13 and τ_0 in the range of 10^{-10} to 10^{-13} s [61,64]. In this paper, the best-fitting parameters were estimated to be $T_{SG} = 82.7$ K, $zv = 1.89$, and $\tau_0 = 0.46 \times 10^{-4}$ s. The obtained higher value of τ_0 and lower value of zv implies a cooperative slower spin flipping, attributed to the presence of randomly oriented FM clusters [61,65]. The CG behavior is probably due to the competing magnetic interactions between Co and Fe ions. Lastly, no apparent frequency dispersion at any other range temperature is shown in Figs. 4(a) and 4(b). Instead, we note only faint features in the phase component output of the ac susceptibility ~95 K [see Fig. 4(b)], indicating an absence of any reentrant SG behavior [61,63,66].

To clarify the FM behavior present in the $NdSrCoFeO_6$ sample, we analyzed the measurement at 10 Oe of the inverse susceptibility χ^{-1} (H/M) as a temperature function, as shown in Fig. 3(b). It was found that the susceptibility thoroughly obeys the Curie-Weiss (CW) law $\chi = C/T - \Theta_{CW}$, with CW temperature $\Theta_{CW} = 130$ K and Curie constant $C = 3.2 \times 10^{-4}$ emu K/g Oe, at high temperatures. The positive value of Θ_{CW} confirms FM ordering at low temperatures in the $NdSrCoFeO_6$ sample. Note that the Θ_{CW} value is lower than the corresponding T_C value, which indicates the presence of short-range order. However, <~245 K (known as the Griffiths phase temperature, T_{GP}), the $\chi^{-1}(T)$ curve starts to deviate from linear behavior and shows a downward curvature in the region $T_C < T < T_{GP}$. According to Das *et al.* [15], this faster decrease of $\chi^{-1}(T)$ in the PM state is attributed to the formation of short-range FM clusters. This behavior can be associated with the existence of the GP, which is often reported in the FM perovskite structure with inhomogeneous magnetic states [15,51,67,68]. According to Pal *et al.* [10], the presence of the GP can occur from disorders associated with the random distribution of Co and Fe ions at site $4b(0.5; 0; 0)$ in the DP structure. Moreover, the spin-canted AFM/FM interaction competitions create random exchange interactions, which can also originate a GP. However, Silva *et al.* [20] suggested that this appearance of the GP is probably caused by the magnetic dilution inherent to nonmagnetic Co^{3+} (LS) ions, which makes it difficult to form long-range order. Additionally, we believe that the natural octahedral distortions in our $NdSrCoFeO_6$ sample can be responsible for changes in

the short- and long-range superexchange interactions (which are competing), which play an important role in the GP observation.

To confirm this observation, the magnetization measurements (M-T) were conducted under different applied fields ($H_{dc} = 0.01$–10 kOe) and plotted as $\chi^{-1}(T)$ curves, as shown in the inset of Fig. 3(b). It is observed that the abnormal downturn in $\chi^{-1}(T)$ curves below T_{GP} can be suppressed gradually by increasing the applied field (disappearing in the 10 kOe curve). This suppression can be interpreted by the increasing PM background and/or the saturated FM component, which could hide the WFM signal [51]. Usually, the characteristics of the GP are described by the following power law relation [15,20]:

$$\chi^{-1} \approx A\left(T - T_C^R\right)^{1-\lambda}, \tag{2}$$

where T_C^R is the critical temperature below which χ diverges, behaving as a simple PM, and λ is an exponent such that $0 < \lambda < 1$ for $T_C^R < T < T_{GP}$ and $\lambda = 0$ for $T > T_{GP}$. The blue line in Fig. 3(b) is the best fitting by the GP model to the $\chi^{-1}(T)$ data, according to Eq. (1). In the case of the $NdSrCoFeO_6$ sample, Θ_{CW} obtained by the CW fitting of the PM region lies below the FM ordering ($\Theta_{CW} < T_C$); we have followed the same approach as used by Pal *et al.* [69] by taking $T_C^R = T_C$, resulting in $\lambda = 0.74$, which confirms the GP. This value lies within the range found for similar DP compounds [10,20–22,69,70]. Therefore, the dynamical freezing point at ~83 K, along with a GP at ~245 K [see Fig. 3(b)], was clearly established in this paper.

The estimated value of the experimental effective magnetic moment $(\mu_{eff})_{exp}$ is 5.06 μ_B for $H_{dc} = 10$ Oe, obtained from the Curie constant by $\mu_{eff} = 2.828\sqrt{C}$ [65]. Increasing H_{dc}, the slope of CW adjustment decreases, indicating a scenario where the Curie constant and CW temperature are field dependent. Thus, at 10 kOe, the effective magnetic moment for the $NdSrCoFeO_6$ sample is $\mu_{eff} = 5.44\,\mu_B$, which is very close to the value of 5.53 μ_B found by de Oliveira *et al.* [13] for the Nd_2CoFeO_6 sample. Recently, XPS analysis performed by Sahoo *et al.* [11] has demonstrated that, in $LaSrCoFeO_6$ crystal, the Co and Fe ions assume 3+ and 4+ valences considering the spin-only moment.

Moreover, authors of previous reports showed that compounds containing Fe and Co can possess complex valence states, and Fe-O-Co double-exchange-type interactions favor electronic transfers from Co intermediate-spin to Fe HS state configurations [17–19]. Interestingly, considering only the combinations assuming 50% of Fe and Co with valence 4+, the magnetic moment can be calculated by interactions Co^{4+} (LS, $S = \frac{1}{2}$), Fe^{4+} (HS, $S = 2$) with Co^{4+} (LS, $S = \frac{1}{2}$), Fe^{4+} (HS, $S = 2$) at different sites, getting $\mu = 5.19\,\mu_B$ for Sr_2FeCoO_6 [17]. However, this consideration does not support load balancing in the $NdSrCoFeO_6$ structure due to the presence of Nd^{3+} sharing the same Sr^{2+} site. The Fe^{3+}/Fe^{4+} in the $NdSrCoFeO_6$ sample was initially analyzed by ^{57}Fe-Mössbauer spectroscopy at room temperature, as shown in Fig. 5(a). This figure shows that the spectrum was deconvoluted into two doublets with different isomer shifts and quadrupole splitting (QS). Doublet 1 with isomer shift (0.05 mm/s) and QS (0.17 mm/s) values are assigned to Fe^{4+} ions (90.8%), while Doublet 2 with isomer shift (0.33 mm/s) and QS (0.13 mm/s) values can be attributed to Fe^{3+} ions (9.2%), both in the LS state [71]. Furthermore, the slight QS values for the Fe ions in the $NdSrCoFeO_6$ sample suggest a strong distorted octahedral Fe site, which is like other DPs such as Pr_2FeCrO_6 [14], $SrLaFeSnO_6$ [72], Sr_2FeCoO_6 [73], and Dy_2FeCoO_6 [8]. This confirms that the $NdSrCoFeO_6$ sample has a noncubic structure, exhibiting only one crystallographic position for the Co/Fe ions, corroborating our results from HRTEM and Rietveld refinement (see Table I).

Furthermore, the XPS technique was employed to determine the chemical states of Nd, Sr, Fe, Co, and O elements in the $NdSrFeCoO_6$ DP. The core-level XPS spectrum of Nd $3p_{5/2}$ shown in Fig. 5(b) can be split into two components. The contribution located at 981.7 eV can be assigned to Nd^{3+} (2.3 at. %), while the second contribution located at 977.9 eV can be ascribed to a shake-down satellite of the Nd $3d^9\,4f^4$ second final state [74,75]. Figures 5(c) and 5(d) shows the core-level spectra of Fe $2p$ and Co $2p$, respectively. Through cautiously deconvoluting, we distinguish two doublets of $2p_{3/2}$ and $2p_{1/2}$ electron levels due to the spin-orbital coupling. The peaks appearing at 709.7 and 723.2 eV correspond to Fe^{3+} (percentage contributions 1.7 at. %), while the components at 711.7 and 725.4 eV are assigned to Fe^{4+} (2.1 at.%) [76]. Additionally, a satellite peak at 715.1 eV indicates the Fe^{3+} valence state [77], confirming that a mixed Fe^{3+}/Fe^{4+} (0.83%) state was found in $NdSrFeCoO_6$, in good agreement with the Mössbauer spectroscopy results. The peaks at 779.9 and 795.1 eV can be attributed to Sr^{2+} (2.6 at. %), whereas the peaks occurring at 781.7 and 796.7 eV can be ascribed to Co^{3+} (2.3 at. %) [76]. The presence of a satellite at 786.2 eV is due to the PM nature of Co^{2+} ions [78,79], confirming a mixed Co^{2+}/Co^{3+} (1.15%) state exist in the $NdSrFeCoO_6$ sample. The core-level XPS spectrum of Sr shown in Fig. 5(e) depicts a doublet signal with binding energies of 133.1 eV (Sr $3d_{3/2}$) and 131.4 eV (Sr $3d_{5/2}$) assigned to Sr^{2+} ions at the A site of the $NdSrFeCoO_6$ lattice (8.0 at. %) [79,80], while the peak at 134.7 eV is ascribed to undercoordinated Sr in the Nd/Sr-O-type termination layer (Sr_{layer}: 1.2 at. %) on the surface of the $NdSrFeCoO_6$ sample [81–83]. Figure 5(f) shows the O $1s$ core-level spectrum, where an asymmetric peak is deconvoluted in four components. The lowest binding energy peak at 528.3 eV may be ascribed to oxygen ions bonded to Nd/Sr at the A site and Fe/Co at the B site of the $NdSrFeCoO_6$ lattice (O_{latt}: 18.3 at. %) [84,85], and the highest binding energy peak at 531.6 eV is associated with an Nd/Sr-O-type $NdSrFeCoO_6$ termination layer (O_{layer}: 29.2 at. %) [86,87]. The peak that appeared at 530.7 eV corresponds to surface oxygen vacancy defects and adsorbed oxygen species, i.e., O^-, O^{2-}, and OH^-, ($O_{V\text{-}ads}$: 32.9 at. %) [80,88], which is consistent with the HRTEM and Mössbauer spectroscopy results. The peak that occurred at 529.5 eV could be ascribed to main lattice oxidative oxygen species ($O_2{}^{2-}/O^-$: 2.7 at. %) [84,87], which are believed to be mainly long-range ordered defect structures, as oxygen vacancies located at the BO_δ layers, which is induced by slightly higher distribution of Co^{2+}/Co^{3+} ions than Fe^{3+}/Fe^{4+} ions at B/B′ sites.

Based on the Mössbauer and XPS investigation, we interpret the FM exchange in the $NdSrFeCoO_6$ sample by valence fluctuations according to the equilibrium

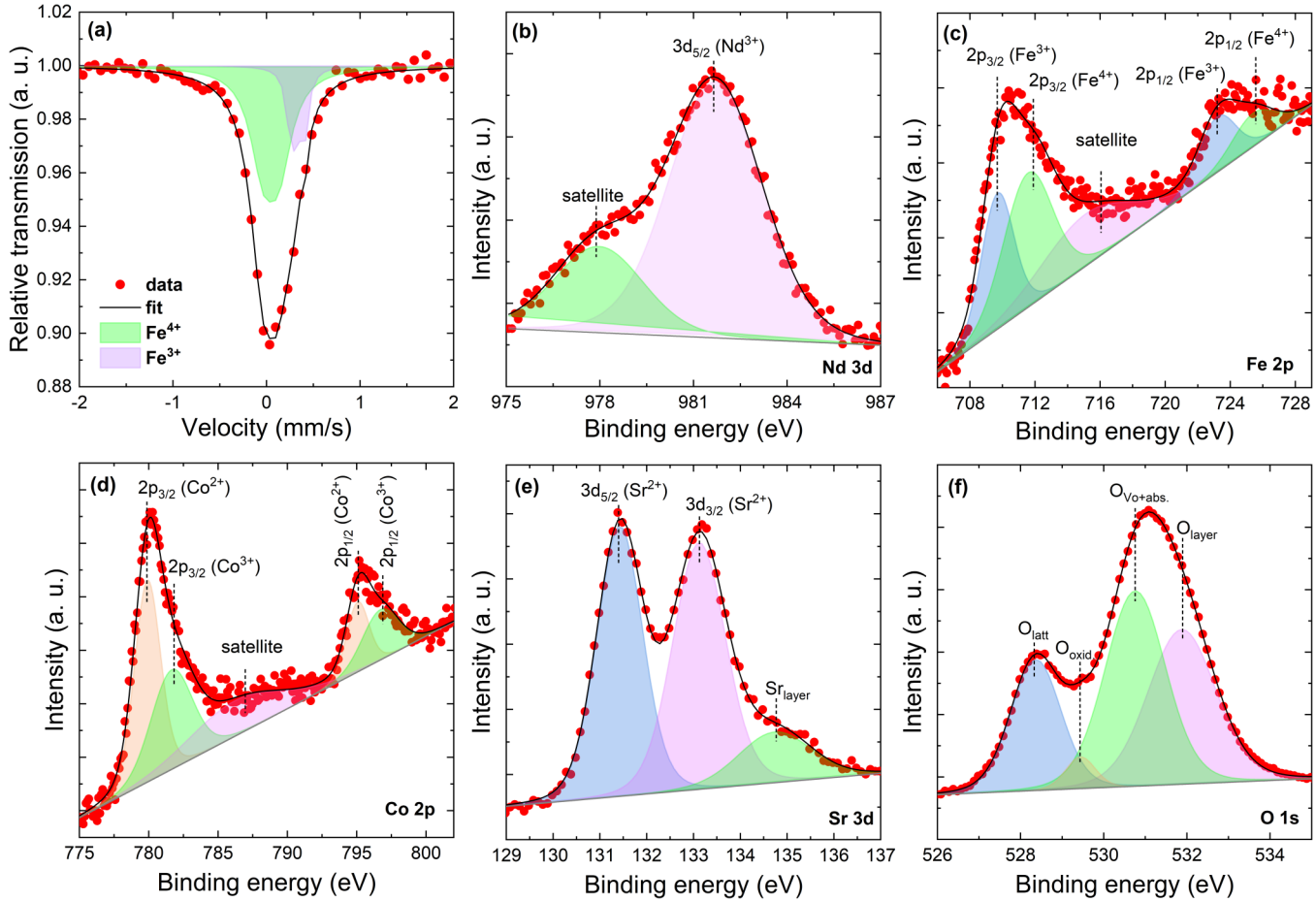

FIG. 5. (a) Room-temperature ^{57}Fe-Mössbauer spectrum and x-ray photoelectron spectroscopy (XPS) spectra of (b) Nd 3*d*, (c) Fe 2*p*, (d) Co 2*p*, (e) Sr 3*d*, and (f) O 1*s* levels for the $NdSrCoFeO_6$ double perovskite.

$Fe^{3+}+Co^{2+} \rightleftharpoons Fe^{4+} + Co^{3+}$. Additionally, authors of recent reports [89,90] have shown that, for the $LaBaCo_2O_{5.5+\delta}$ and $NdBaCoFeO_{5+\delta}$ samples, Co/Fe at the B site is expected to show valence 3+/4+ when the A site contains two ions with valences 3+/2+ (La/Nd, Ba). Notably, the Co^{3+} spin-state degeneracy fluctuations are possible because the crystal-field splitting between t_{2g} and e_g has energy very close to Hund's exchange coupling. Thus, possible thermal perturbations can induce electronic transfer to e_g orbitals, increasing the exciting Co^{3+} states [91,92]. Complementarily, this assumption is valid since, for these types of materials, the transition to a PM state involves a thermally driven spin-state crossover of Co^{3+} ions, entailing a transition from the diamagnetic ground state with LS configuration ($t_{2g}^6 e_g^0$, $S = 0$) to an excited intermediate-spin state ($t_{2g}^5 e_g^1$, $S = 1$) [13]. Thus, we considered the HS and LS states for the $Nd^{3+}/Fe^{3+}/Co^{2+}$ and Fe^{4+} ions, respectively, while Co^{3+} was in the possible HS, intermediate-spin, and LS states. Consequently, the magnetic moment can be calculated as follows:

$$\mu_{\text{theo}}^2 = [(\mu_{Nd^{3+}})^2 + (0.6\mu_{Co^{2+}} + 0.52\mu_{Co^{3+}})^2 + (0.4\mu_{Fe^{3+}} + 0.48\mu_{Fe^{4+}})^2]\mu_B, \quad (3)$$

where the $\mu_{Nd} = g_J\sqrt{J(J+1)}\mu_B$ (spin-orbit coupling) and $\mu_{Co/Fe} = g\sqrt{S(S+1)}\mu_B$ (spin-only interaction) values are listed in Table II. The experimental value of $\mu_{\text{eff}} = 5.44\,\mu_B$ (at 10 kOe) obtained by CW adjustment suggests the possible coexistence of Co^{3+} ions in the HS and intermediate-spin states with $\mu_{\text{theo}} = 6.63\,\mu_B$ and $\mu_{\text{theo}} = 5.88\,\mu_B$, respectively. Since a pure Co^{3+} HS state ($S = 2$) would lead to a saturation magnetization of $\sim 4.9\,\mu_B$ to be compared with a measured value of $1.7\,\mu_B$, the cobalt spin state is either lower (intermediate spin, $S = 1$; $M_S = 2\,\mu_B$), or the different cobalt sites show different spin states whose combination yields the measured value. This result suggests an induced exchange interaction between Co^{2+} ($t_{2g}^5 e_g^2$) (HS, $S = \frac{3}{2}$) and Fe^{3+} ($t_{2g}^3 e_g^2$) (HS, $S = \frac{5}{2}$), as well as Co^{3+} ($t_{2g}^4 e_g^2$) (HS, $S = 2$)/Co^{3+} ($t_{2g}^5 e_g^1$) (intermediate spin, $S = 1$) and Fe^{4+} ($t_{2g}^4 e_g^0$) (LS, $S = 1$) in the $NdSrCoFeO_6$ sample, whereas disordered crystallographic occupation and mixed valences between Co and Fe ions induced mixed FM and AFM interactions which led to inhomogeneous magnetic behavior in the $NdSrCoFeO_6$ sample [93].

To further confirm the magnetic state of the $NdSrCoFeO_6$ sample, isothermal magnetization (M-H) measurements were collected at three different temperatures of 2 K (up to 10 kOe) and 80 and 300 K (up to 40 kOe), as shown in Fig. 6. Here, M-H loops were observed at 2 and 80 K ($T < T_C$), which indicates the overall FM nature of the sample. However, the PM behavior was confirmed at 300 K ($T > T_C$).

TABLE II. Effective magnetic moment calculated for different combinations of Co^{2+}/Co^{3+} and Fe^{3+}/Fe^{4+} ions obtained by XPS analysis.

Nd^{3+} (μ_B)	(0.4)Fe^{3+} (μ_B)	(0.48)Fe^{4+} (μ_B)	(0.52)Co^{3+} (μ_B)	(0.6)Co^{2+} (μ_B)	$\mu_{theo}(\mu_B)$
$J = \frac{9}{2}$ (HS)	$S = \frac{5}{2}$ (HS)	$S = 1$ (LS)	$S = 2$ (HS)	$S = \frac{3}{2}$ (HS)	6.63
			4.90	3.87	
3.62	5.92	2.82	$S = 1$ (intermediate-spin)		5.88
			2.82		
			$S = 0$ (LS)		5.07
			0.00		

Considering that the Co and Fe spins are aligned in the same directions with $Fe^{3+}/Fe^{4+}/Co^{2+}$ in an HS state and Co^{3+} in an intermediate-spin/HS state (as previously suggested), a magnetization of 2.25 μ_B at 10 kOe for $NdSrCoFeO_6$ at low temperature (2 K) was observed. The difference between this value of 2.25 μ_B and that obtained by CW adjustment of 5.44 μ_B can be attributed to a possible canting of spins due to the low field used in this measure. Moreover, the magnetic moment is significantly reduced probably by the ASD effect present in the system, creating an antiparallel orientation of the Co^{3+}-Fe^{4+} and Co^{2+}-Fe^{3+} ion pairs ferromagnetically coupled in the lattice, which imply in a simultaneous reduction in the average magnetic moments of these sublattices and are transferred to the total magnetic moment [11,94]. The existence of mixed-valence states of Co (Co^{2+}/Co^{3+}) and Fe (Fe^{3+}/Fe^{4+}) due to Sr^{2+} doping at the Nd^{3+} site can also cause a decrease in magnetization [11], and this scenario will be considered later through DFT analysis.

C. Electrical resistivity

Figure 7(a) shows the temperature-dependent resistivity $\rho(T)$ curve of the $NdSrCoFeO_6$ sample measured under fields of 0 and 100 Oe in the temperature range of 150–300 K. The sample exhibits a semiconductinglike behavior like other DPs [7,13,46]. Generally, the electrical transport behavior of semiconductors could be described by three models: thermal activation (TA), small-polaron hopping (SPH), and variable range hopping (VRH) [51], which are described by the expressions $\rho_{TA} = \rho_0 \exp(E_A/k_B T)$, $\rho_{SPH}/T = A\exp(E_A/k_B T)$, and $\rho_{VRH} = \rho_0 \exp(T_0/T)^{1/4}$, respectively. Herein, A is a constant, and ρ_0, E_A, k_B, and T_0 are the residual resistivity, activation energy, Boltzmann constant, and characteristic temperature, respectively. The linear fitting results from the TA, SPH, and VRH models are shown in Figs. 7(b)–7(d), which yields the parameters $\rho_0 = 0.056\,\Omega\,m$ and $E_A = 0.174$ eV, $\rho_0 = 0.009\,\Omega\,m$ and $E_A = 0.203$ eV, and $\rho_0 = 0.129\,\Omega\,m$ and $T_0 = 0.89$ K, respectively. The activation energy to the VRH model can be calculated from the equation $E_A = \frac{k_B}{4} T_0^{1/4} T^{3/4}$ [46]. The calculated value varies from 0.001 to 0.002 eV as temperature increases from 150 to 300 K. Usually, in disordered systems, resistivity follows different conduction mechanisms with a change in slope of the $\rho(T)$ curve around a charge localization temperature [95]. As can be seen in Figs. 7(b) and 7(c), the linear fitting does not work very well following the TA and SPH models in the low-temperature region. On the other hand, from the VRH model fitting displayed in Fig. 7(d), the curve follows the linearity over almost the entire temperature range, indicating the best model for describing the conduction mechanism in the sample. As it is already known, the random distribution of Co and Fe ions at the B/B′ site in the orthorhombic $NdSrCoFeO_6$ DP leads to 3D disorder in the structure, weakening the double-exchange interaction and the possibility of e_g electron hopping between the random magnetic clusters [51]. Then hopping conduction in a band of localized states may be possible without electron-electron interactions [96]. Therefore, the semiconducting behavior of the $NdSrCoFeO_6$ sample can be interpreted better by the VRH model.

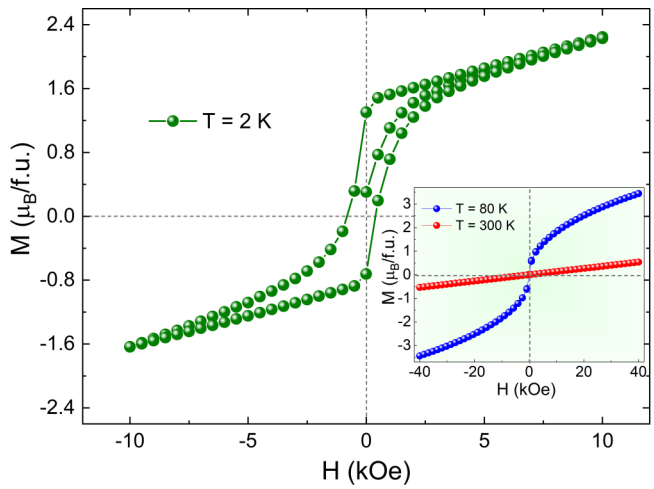

FIG. 6. M-H magnetic hysteresis loop is shown for the $NdSrCoFeO_6$ sample at 2 K measured under a magnetic field up to 10 kOe. The inset shows M-H loops at 80 and 300 K up to 40 kOe.

D. MCE studies

The MCE study provides a powerful tool to enquire about magnetic transitions. Thus, a series of isothermal magnetization curves (M-H) were recorded in a large temperature range of $130 < T < 170$ K with temperature interval $\Delta T = 2$ K under fields up to 40 kOe, as shown in Fig. 6(a). The magnetization rapidly increases at low field values and then linearly increases up to the highest measuring field of 40 kOe without showing any saturation tendency. The nature of the M-H curves is also attributed to the coexistence of weak FM (low-field) and canted AFM (high-field) states. Above T_C, the magnetization increases almost linearly in the scanning field range, ascribed to the PM ground state. The M-H isotherms have been transformed into Arrott plots (M^2 vs H/M) [97,98], which are shown in the inset of Fig. 8(a). The positive

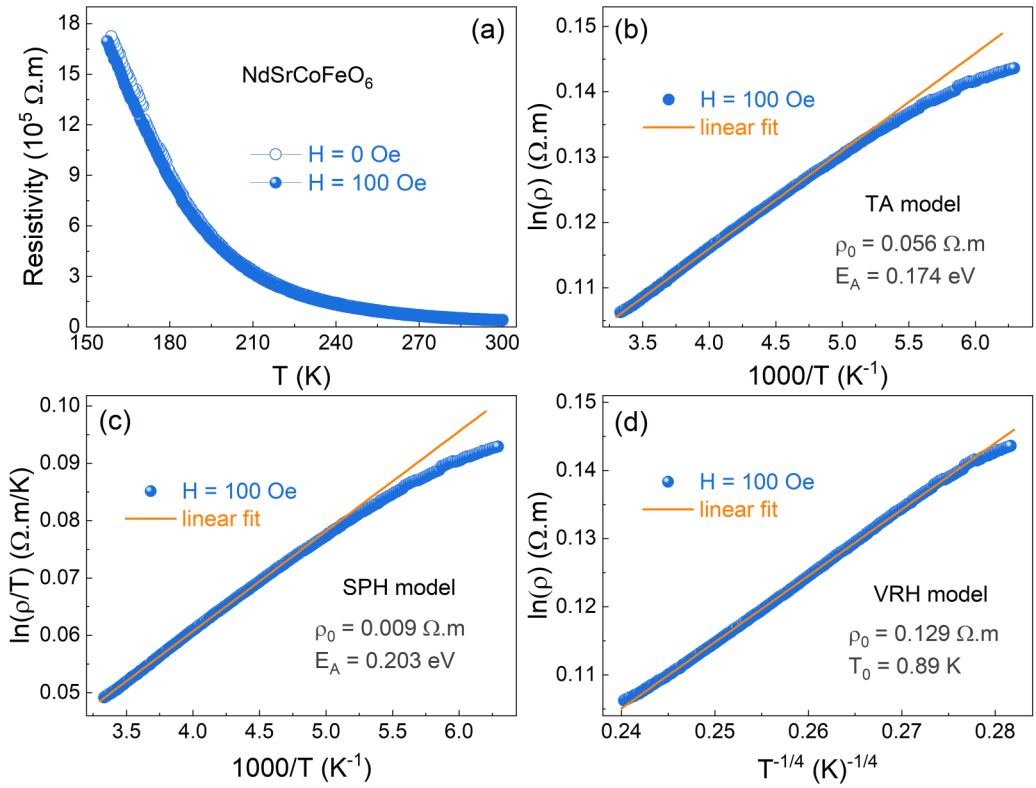

FIG. 7. (a) Temperature-dependent resistivity $\rho(T)$ curve, (b) $\ln(\rho)$ vs T^{-1} fitting to thermal activation (TA) model, (c) $\ln(\rho/T)$ vs T^{-1} fitting to small-polaron hopping (SPH) model, and (d) $\ln(\rho)$ vs $T^{-1/4}$ fitting to variable range hopping (VRH) model for the $NdSrCoFeO_6$ sample.

slope of the Arrott plots over the whole measuring temperature range indicates that the FM transition is a second-order phase transition (SOPT) [99], indicating that our results are in agreement with previously reported MCE in other DP compounds [16,23,100].

Based on Maxwell's thermodynamic relation, the change in magnetic entropy $(-\Delta S_M)$ for any magnetic material under a variation of the applied magnetic field from 0 to $H_{\max}$ can be expressed as [101–103]

$$|\Delta S_M(T,H)| = \int_0^{H_{\max}} \left(\frac{\partial M}{\partial T}\right)_H dH. \tag{4}$$

However, for magnetization measurements with small discrete field and temperature intervals, ΔS_M can be approximately calculated as

$$\Delta S_M(T,H_0) = \sum_i \frac{M_{i+1}\text{-}M_i}{T_{i+1}\text{-}T_i}\Delta H_i, \tag{5}$$

where M_i and M_{i+1} are the experimental data obtained at temperatures T_i and T_{i+1}, under a magnetic field H_i, respectively [104,105]. The temperature dependence with $-\Delta S_M$ for different magnetic fields is shown in Fig. 8(b). All curves show positive values in the entire measuring temperature region and exhibit a peak around T_{C1} (∼150 K), with the peaks broad asymmetrically on both sides as increasing fields. The maximum value of entropy change $-\Delta S_M^{\max}$ of $1.84\,\mathrm{J\,kg^{-1}\,K^{-1}}$ was observed near the second FM-PM transition temperature (T_{C2}) for the $NdSrCoFeO_6$ sample under an applied field of 40 kOe. The occurrence of $-\Delta S_M^{\max}$ below the FM-PM transition temperature can be associated with the incomplete ordering of the Nd^{3+} RE ions [16,58]. Moreover, the existence of magnetic competition or frustration between the FM and canted AFM ordering and long-range ordering of Nd^{3+} ions may be a possible reason for such a value of $-\Delta S_M^{\max}$ in the $NdSrCoFeO_6$ sample [100,106]. This value of $-\Delta S_M^{\max}$ is lower than that for other Co/Fe-based DPs with 8.85 and $7.82\,\mathrm{J\,kg^{-1}\,K^{-1}}$ for Er_2FeCoO_6 and Gd_2FeCoO_6, respectively [23]. However, it is somewhat larger than other DP compounds, such as Nd_2CrMnO_6 ($1.3\,\mathrm{J\,kg^{-1}\,K^{-1}}$) [107] and Sm_2CoMnO_6 ($1.4\,\mathrm{J\,kg^{-1}\,K^{-1}}$) [108]. Likewise, in the MCE behavior for the Gd_2CoMnO_6 DP that was reported by Das *et al.* [15], we observed that $\Delta S_M^{\max}$ follow a power law behavior as $\Delta S_M^{\max} \approx H^n$, as shown in the inset of Fig. 8(b), where $\Delta S_M^{\max}$ increases almost linearly with H, being $n \sim 1$. Moreover, it is worth mentioning that other DP compounds also have a value of n close to 1 [55,100,108]. Differently, Das and Mazumdar [16] do not report linearity in $\Delta S_M^{\max}$ as a function of H for Pr_2FeCrO_6. Their presented values of n were between 1.28 and 1.67, which can be assigned to the presence of WFM interactions and canted AFM states. Thus, our value of n close to 1 confirms the presence of FM ordering in the $NdSrCoFeO_6$ sample. The relative cooling power (RCP) is the most meaningful parameter used to evaluate the cooling efficiency of magnetic materials designed for applications in magnetic refrigeration [24]. To check the RCP of the $NdSrCoFeO_6$ sample, we consider the shape and width of $-\Delta S_M(T)$ curves, through the expression $\mathrm{RCP} = |\Delta S_M^{\max}|\delta T_{\mathrm{FWHM}}$, where δT_{FWHM} is the full width at half

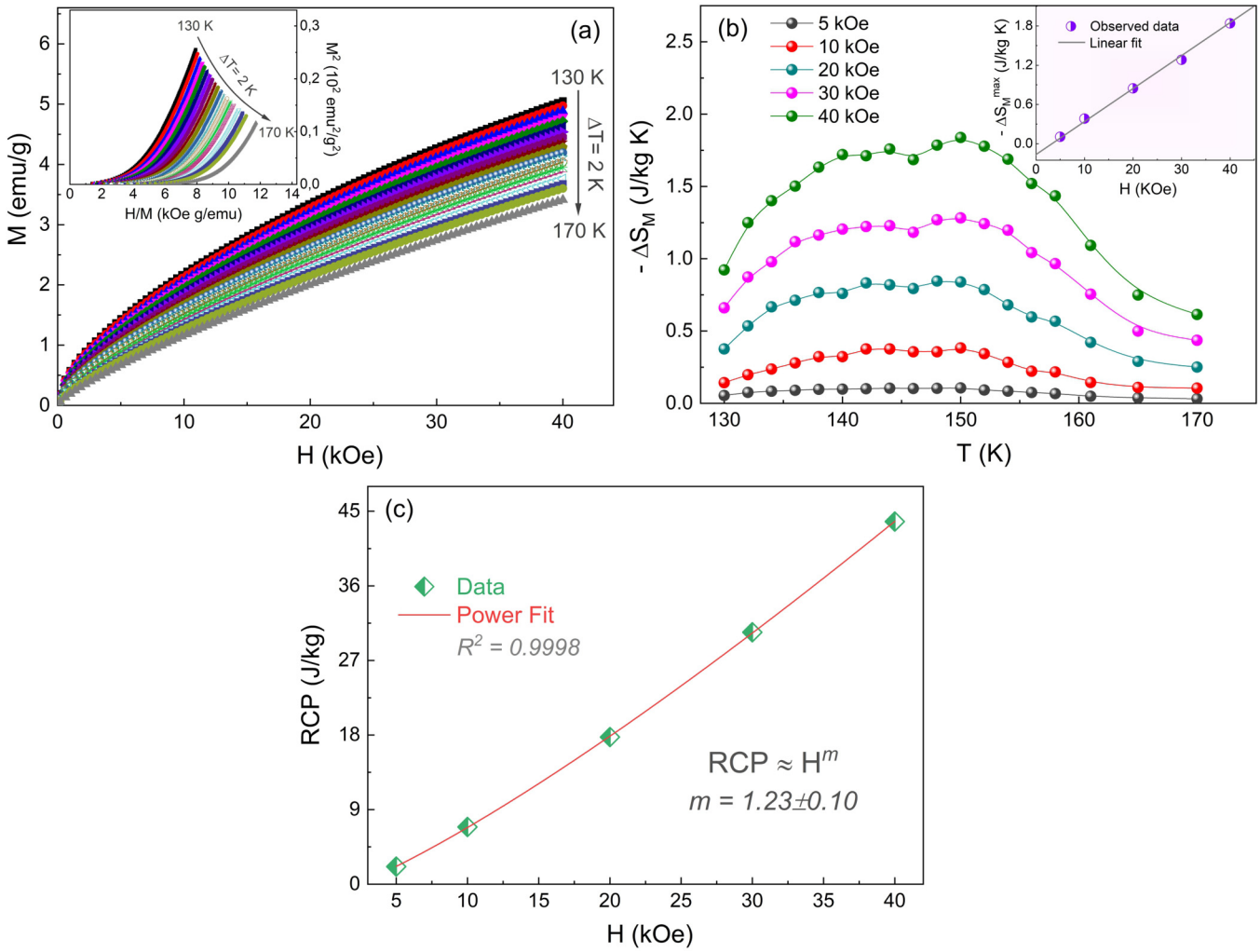

FIG. 8. (a) Isotherms M-H measured at different temperatures from 130 to 170 K, inset is the Arrott plots (M^2 vs H/M). (b) Dependence of $-\Delta S_M$ with temperature taken at different magnetic fields from 5 to 40 kOe. Inset shows H dependence of maximum magnetic entropy ($-\Delta S_M^{\max}$). (c) Relative cooling power (RCP) as a function of the magnetic field.

maximum of the $-\Delta S_M(T)$ curves [104]. The RCP variation as a function of the magnetic field is presented in Fig. 8(c). Obviously, an increase in RCP is observed when the magnetic field increases, which follows a power law as RCP $\approx H^m$, where m is the power exponent. The adjusted data yield $m = 1.23 \pm 0.10$. Moreover, we observe an RCP maximum value of 43.8 J kg^{-1} at 40 kOe, which is smaller than several DP compounds [58,100,107,109–111]. However, this value has a magnitude two times smaller than RCP $\approx$ 85 J kg^{-1} under a field of 40 kOe observed for a quasi-one-dimensional hexagonal ferromagnet $PrCrGe_3$ [24]. Therefore, the $NdSrCoFeO_6$ sample can be a candidate potentially fruitful for theoretical studies and practical applications, working in a wide temperature range.

E. Critical behavior

To get further insights into the FM-to-PM transition and the existence of the GP, we investigated in detail the critical behavior characterized by the critical exponents. The critical behavior of a SOPT material could be analyzed by the critical exponents β, γ, and δ, which are defined as [15,107,112]

$$M_S(0,\epsilon) \sim (-\epsilon)^{\beta}, \quad \epsilon < 0, \quad T < T_C, \tag{6}$$

$$\chi_0^{-1}(0,\epsilon) \sim (\epsilon)^{\gamma}, \quad \epsilon > 0, \quad T > T_C, \tag{7}$$

$$M(H,0) \sim (H)^{1/\delta}, \quad \epsilon = 0, \quad T = T_C, \tag{8}$$

where $\epsilon = (T - T_C)/T_C$ is the reduced temperature. All three exponents β, γ, and δ are not independent of each other, and the Widom scaling relation predicts that $\delta = 1 + \gamma/\beta$ [113]. According to the Arrott-Noakes equation of state, which is described as $(H/M)^{1/\gamma} = a\epsilon + b(M)^{1/\beta}$ (a and b are constants), the modified Arrott plot (MAP) by $(M)^{1/\beta}$ vs $(H/M)^{1/\gamma}$ curves with proper β and γ values near T_C should produce a set of parallel straight lines, and the isotherm at the T_C line could pass the origin of coordinates [97,107]. Landau's mean-field theory ($\beta = 0.5$ and $\gamma = 1.0$) shows that the M^2 vs H/M curves at various temperatures around T_C should be a series of parallel lines in the high-field region [24]. However,

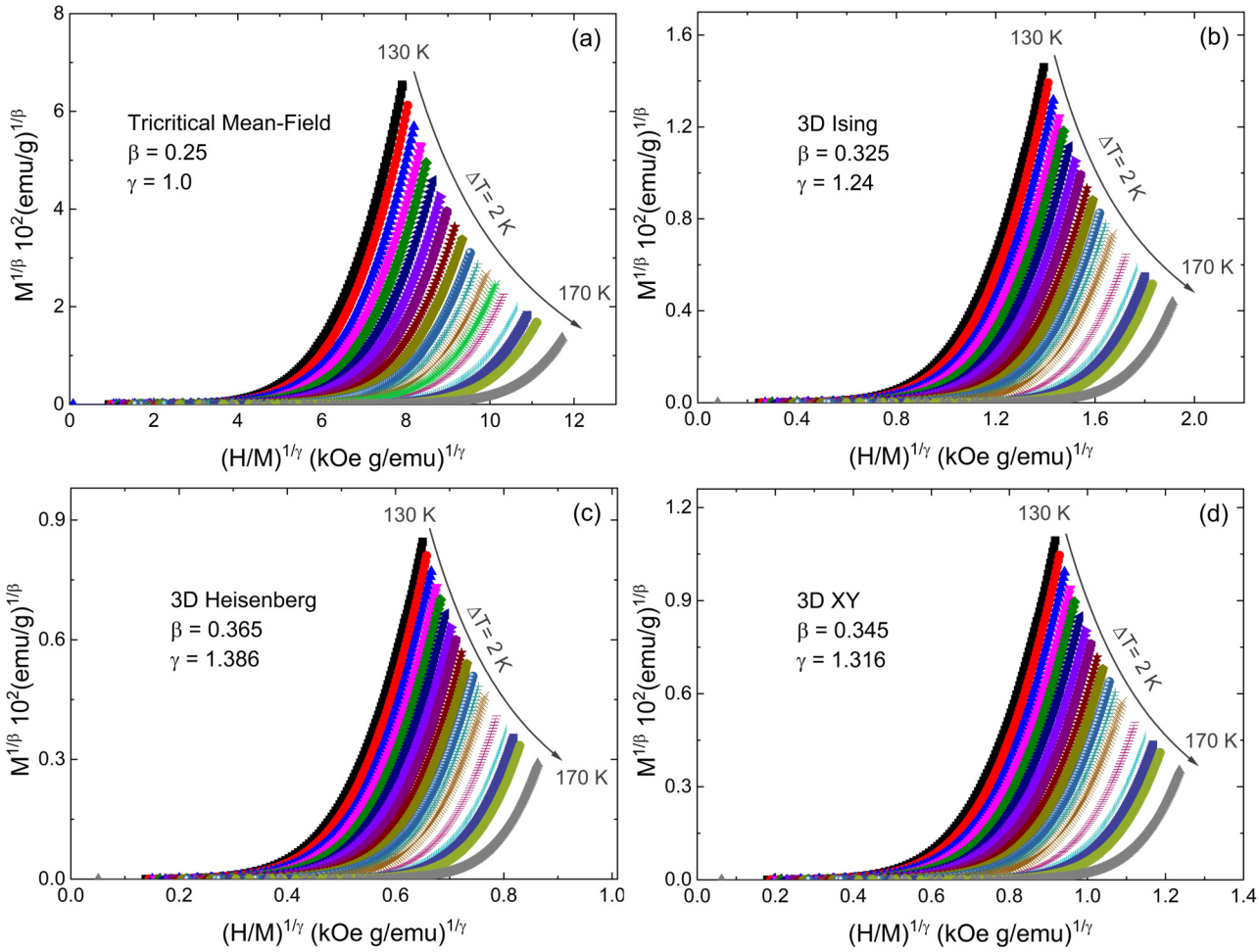

FIG. 9. Modified Arrott isotherms plotted as $M^{1/\beta}$ vs $(H/M)^{1/\gamma}$ with (a) tricritical mean-field model, (b) three-dimensional (3D) Ising model, (c) 3D Heisenberg model, and (d) 3D XY model.

the M^2 vs H/M curves shown in the inset Fig. 8(a) are not strictly linear in the high-field region, which indicates that the mean-field model cannot characterize the critical behavior for the $NdSrCoFeO_6$ sample. Thus, the tricritical mean-field model ($\beta = 0.25$, $\gamma = 1.0$), 3D Ising model ($\beta = 0.325$, $\gamma = 1.24$), 3D Heisenberg model ($\beta = 0.365$, $\gamma = 1.386$), and 3D XY model ($\beta = 0.345$, $\gamma = 1.316$) were used to establish the MAP [24,104], which are exhibited in Fig. 9. All models exhibit quasistraight lines in high field, making it difficult to identify the most appropriate model. To find the best model, it was essential to calculate the relative slope (RS), defined by $\mathrm{RS} = S(T)/S(T_C)$, where $S(T)$ and $S(T_C)$ are the slopes determined from the MAP near and at T_C, respectively. In an ideal model, the MAP consists of a series of parallel straight lines, i.e., RS should equal 1. However, from the RS vs T curves shown in Fig. 10(a), we can see that these universality classes could not clearly describe the critical behavior of the $NdSrCoFeO_6$ sample.

We used the iteration method to obtain the correct critical exponents β and γ [24,114,115]. The convergence in the MAP fitting $(M)^{1/\beta}$ vs $(H/M)^{1/\gamma}$ is achieved for $\beta = 1.384$ and $\gamma = 0.621$, as shown in Fig. 10(b). Usually, the values of critical exponents (β and γ) for several DPs are close to that for the mean-field model [55,116]. However, our critical exponent values follow a very similar relationship ($\beta \approx 2\gamma$), as observed by Das *et al.* [15] for DP Gd_2CoMnO_6 and are also quite far from any conventional universality class. As expected, the isotherms shown in Fig. 10(b) passed through the origin with $T_C \sim 150$ K, consistent with the T_{C2}=149 K value determined from the $dM_{FC}/dT(T)$ curve. The intersections of isotherms for $T < T_C$ on the $M^{1/\beta}$ axis and for $T > T_C$ on $(H/M)^{1/\gamma}$ axis give the values of spontaneous magnetization M_S and inverse magnetic susceptibility χ_0^{-1}, respectively [117]. Thus, Fig. 10(c) shows the finally obtained values of M_S and χ_0^{-1} as a function of temperature. The power law fitting to $M_S(T)$ and $\chi^{-1}(T)$ according to Eqs. (6) and (7), respectively, reveals $\beta = 1.381 \pm 0.007$ with $T_C = 150.72 \pm 0.02$ K and $\gamma = 0.632 \pm 0.004$ with $T_C = 151.82 \pm 0.02$ K. To determine the exponent δ, we take the log-log plot of $M(H)$ at $T = 150$ K. The straight-line fit gives the exponent $\delta = 1.421 \pm 0.02$, which is shown in the inset of Fig. 10(c). Using the Widom scaling relation $\delta = 1 + \gamma/\beta$ [15,113] and the values of β and γ determined from MAP fitting [Fig. 10(b)], we obtain $\delta = 1.448$. This value is slightly far (2%) from that found by the log-log plot of the $M(H)$ curve of $\delta = 1.421$ [inset Fig. 10(c)], which may be because the chosen curve for fitting at a temperature is slightly different from the ideal at $T_{C2} = 149$ K. Thus, the change in the values of critical expo-

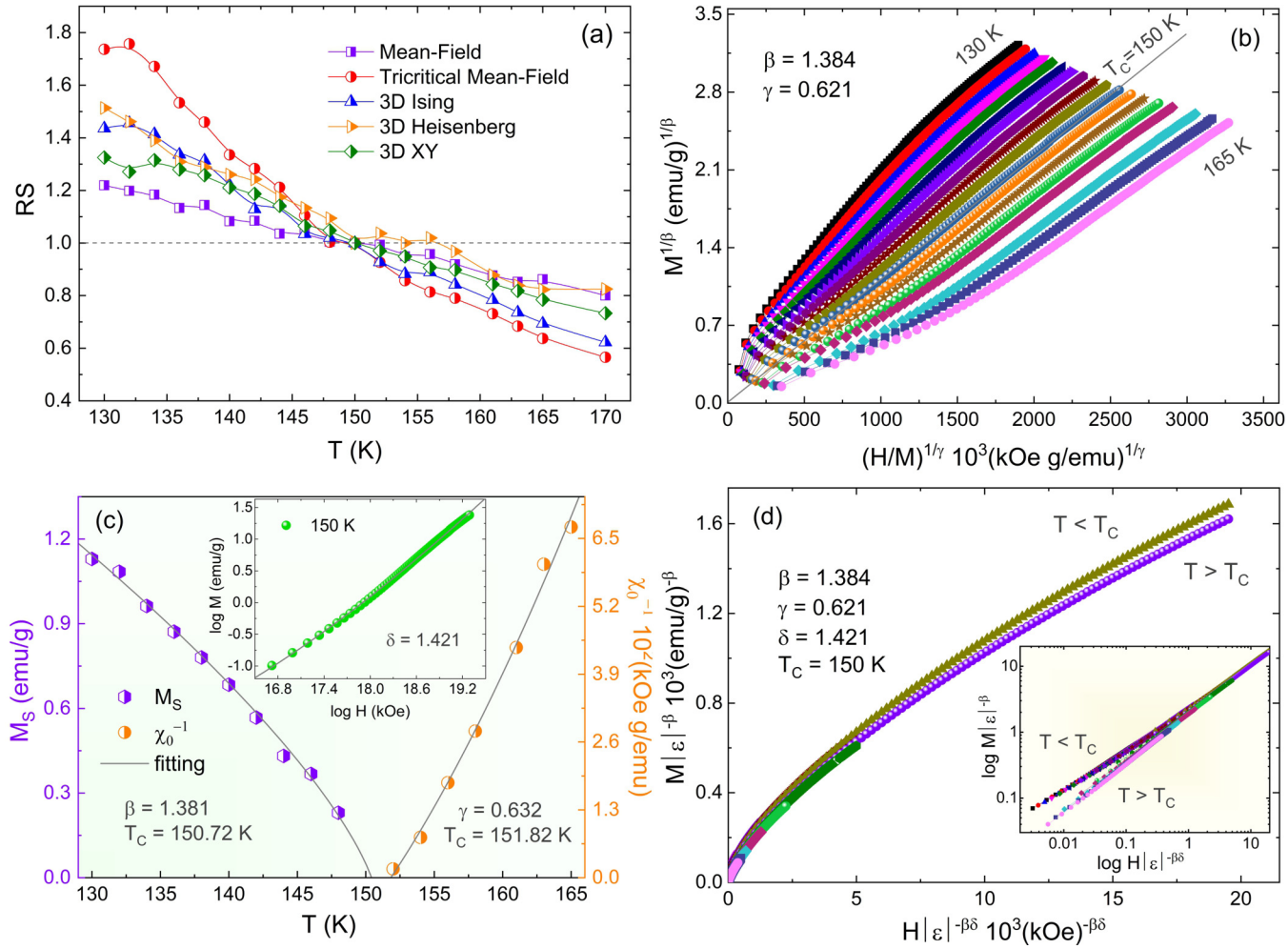

FIG. 10. (a) Temperature dependence of the relative slope (RS). (b) Modified Arrott plot $(M)^{1/\beta}$ vs $(H/M)^{1/\gamma}$ constructed from $M(H)$ data with critical exponents $\beta = 1.384$ and $\gamma = 0.621$. (c) Temperature dependence of spontaneous magnetization (M_S) and initial inverse susceptibility (χ_0^{-1}). The solid gray lines represent the best-fit curve according to Eqs. (6) and (7). The inset shows a log-log plot of $M(H)$ isotherm at 150 K, the nearest one to the critical isotherm. (d) Scaling plots below and above T_C according to Eq. (9). The inset shows the same plot in the log-log scale.

nents is tiny and within our experimental error. The critical exponents of $NdSrCoFeO_6$ are also shown in Table III and compared with other DP compounds and theory model values. From this scaling hypothesis, the reliability of the obtained critical exponents was certified by the magnetic equation of state in the asymptotic critical region, which is expressed as [15,24]

$$M(H,\epsilon) = |\epsilon|^{\beta} f_{\pm}\left(\frac{H}{|\epsilon|^{\beta\delta}}\right). \tag{9}$$

Here, $f_{\pm}$ are regular functions with f_+ for temperatures above T_C and f_- for temperatures below T_C. Using the values of β, δ, and T_C obtained from the MAP, we have constructed the plots of $M|\epsilon|^{-\beta}$ vs $H|\epsilon|^{-\beta\delta}$. The curves clearly collapsed into two different universal curves, one for $T > T_C$ and another for $T < T_C$, as shown in Fig. 10(d). The log-log has also been plotted and shown as an inset in Fig. 10(d). This result confirms that the values of the critical exponents obtained here are reliable and in agreement with the scaling hypothesis. Furthermore, we observed a slight deviation from the scaling curves in the low magnetic field region due to the rearrangement of the magnetic domains, where magnetic moments are not entirely aligned to the applied magnetic field.

Finally, it is known that the universality class of the magnetic phase transition depends on the exchange distance $J(r)$. Theoretically, the magnetic ordering is treated as an attractive interaction of spins, where a renormalization group theory analysis suggests the interaction decays with distance r as [24,113,121]

$$J(r) \approx r^{-(d+\sigma)}, \tag{10}$$

where d is the spatial dimensionality, and σ is a positive constant. Moreover, the susceptibility exponent γ is predicted by considering that the range of spin interaction is long or short depending on $\sigma < 2$ or $\sigma > 2$, by a renormalization group approach [24,114]:

$$\gamma = 1 + \frac{4(n+2)}{d(n+8)}\Delta\sigma + \frac{8(n+2)(n-4)}{d^2(n+8)^2} \times \left[1 + \frac{2G(d/2)(7n+20)}{(n-4)(n+8)}\right]\Delta\sigma^2, \tag{11}$$

TABLE III. Comparison of critical exponents of $NdSrCoFeO_6$ with other DP compounds and theoretical models.

Composition	Reference	T_C (K)	β	γ	δ
$NdSrCoFeO_6$	This paper	149	1.381	0.632	1.421
Nd_2CoMnO_6	[118]	156	0.545	1.131	3.075
Gd_2CoMnO_6	[15]	123	1.18	0.65	1.55
Nd_2CrMnO_6	[107]	80	0.607	0.706	2.01
Eu_2NiMnO_6	[116]	147	0.443	1.014	3.289
Sr_2FeMoO_6	[119]	409	0.388	1.30	4.35
La_2CoMnO_6	[120]	224	0.59	1.12	
Mean field	[24]		0.5	1.0	3.0
Tricritical mean field	[24]		0.25	1.0	5.0
3D Ising	[24]		0.325	1.24	4.82
3D Heisenberg	[24]		0.365	1.386	4.8
3D XY	[24]		0.345	1.316	4.81

where n is the spin dimensionality by $n = 1 + (\beta\text{-}1/\beta + \gamma)$, $\Delta\sigma = \sigma\text{-}d/2$, and $G(d/2) = 3\text{-}\frac{1}{4}(d/2)^2$. For a 3D material ($d = 3$), we have $J(r) \approx r^{-(3+\sigma)}$, with $\frac{3}{2} \leqslant \sigma \leqslant 2$. When $\sigma = 2$, the 3D Heisenberg model ($\beta = 0.365$, $\gamma = 1.386$, and $\delta = 4.8$) is valid for the 3D isotropic magnet, where $J(r)$ decreases faster than r^{-5}. Whereas $\sigma = \frac{3}{2}$, conditions for the mean-field model ($\beta = 0.5$, $\gamma = 1.0$, and $\delta = 3.0$) are satisfied, expecting that $J(r)$ decreases more slowly with $r^{-4.5}$ [113]. Herein, using the values of β and γ as calculated from the magnetization scaling analysis, we deduced self-consistent critical exponents by obtaining $n = 1.192$, in excellent agreement with the previously mentioned experimental value [inset of Fig. 8(b)]. As a result, $\sigma = 1.73$ is obtained according to Eq. (11), implying that the magnetic exchange distance decreases with $J(r) \approx r^{-4.7}$ in the $NdSrCoFeO_6$ sample. This value is consistent with those obtained for several FM materials [24,107,112,122]. Then we can note that $J(r)$ falls between the 3D Heisenberg model and the mean-field model. However, it is closer to the mean-field model, suggesting that the main spin interactions are long-range magnetic interactions. Thus, the existence of competition between long- and short-range magnetic interaction should be responsible for this critical behavior in $NdSrCoFeO_6$ sample.

F. DFT studies

To further investigate the structural and electronic characteristics of the $NdSrCoFeO_6$, we performed DFT calculations [33,34]. The calculations were realized with five different conventional cells containing 20 atoms. The systems were systematically built based on the structural lattice parameters experimentally obtained in this paper through Rietveld refinement (shown in Table I). The double occupancy character of the sites is treated by keeping the concentration of Nd/Sr and Co/Fe fixed. Firstly, we tested the stability of the systems concerning the disorder positions of the Nd and Sr ions. Then cells are simulated interchanging positions of Co and Fe to simulate different chemical environments. Spin-polarized ground states were obtained by computing different magnetic configurations. The most energetically stable structures found are illustrated in Fig. 11 alongside their respective electronic bands. All Co and Fe ions are crystallographically equal for the columnar structure [Fig. 11(c)]. However, the rock-salt type structure [Fig. 11(d)] has two nonequivalent Co and two nonequivalent Fe. All Nd and Sr ions possess the same equivalence for the two cells (more details regarding each simulated system can be found in the Supplemental Material [123]).

Figures 11(a) and 11(b) show the results for the total and partial density of spin-polarized states (TDOS and PDOS, respectively) based on carefully optimized $NdSrCoFeO_6$ crystal structures. We started the calculations by relaxing the structural parameters. The corresponding optimized $a = 5.283$ Å, $b = 7.636$ Å, and $c = 5.403$ Å lattice parameters are equal for both columnar and rock-salt cells. Compared with the experimental results (see Table I), optimized cells show a decrease along the x axis, evidenced by the lower value of the a parameter (-3%), while b and c parameters practically did not change. Firstly, we tested the Nd (↑↑), Co (↑↑), and Fe (↑↑) spin setup in which the calculated values of magnetic moments (μ_B/cell) converged to values of 18 μ_B, which is much higher than the experimental predictions. However, a simulated magnetic ground state was achieved by using the configuration Nd (↑↓), Co (↑↑), and Fe (↑↑), which agrees well with the experimental finds. Therefore, we explored the former system of magnetic moments (μ_B/site) for analysis purposes, whereas the local moments computed at the Co and Fe sites for the columnar structure are 1.67 and 3.77 μ_B, respectively. Average magnetic moments of 1.43 μ_B on Co and 3.87 μ_B on Fe sites were obtained when the rock-salt structure was considered. The reason for the magnetic moment changes comes from an interesting effect: As the number of inequivalent magnetic ions (Co/Fe) increases within the unit cell, the magnetic moment of Co shows a natural tendency to decrease, causing short-range interactions. This is most likely favored by increasing the degree of hybridization between $3d$ and $2p$ states of the neighboring oxygens. At the same time, an opposite behavior can be expected for Fe because increases in its magnetic moment imply a longer-range interaction with its neighbors. Thus, the hybridization between their $3d$ and O $2p$ states will decrease. Another way to verify this behavior is by analyzing the variation of the average bond length for the two structures: 1.90 Å for ⟨Co-O⟩ and 1.93 Å for ⟨Fe-O⟩ in the columnar structure, and 1.88 Å for ⟨Co-O⟩ and 1.95 Å for ⟨Fe-O⟩ in the rock-salt structure. Therefore, it indicates a competition between short- and long-range magnetic interactions, which is responsible for the magnetic behavior in our system. Although DFT does not describe well the properties arising from the localized character of the Nd $4f$ states, this result agrees with the earlier analysis of the magnetic exchange distance $J(r)$ that was calculated using values of critical exponents obtained experimentally. Additionally, the projected magnetic moment for both structures is 2.95 μ_B for the Nd ions, indicating that this computed result is not far from that summarized in Table II.

Figure 11(a) shows the calculated density of electronic states (DOS) of the $NdSrCoFeO_6$ in the columnar cell. Herein, we analyze the orbital character of the energy bands and corresponding contributions of each Nd, Co, Fe, and O. The Sr-state contributions are not shown because they appear in higher-energy regions. As can be observed, a portion of

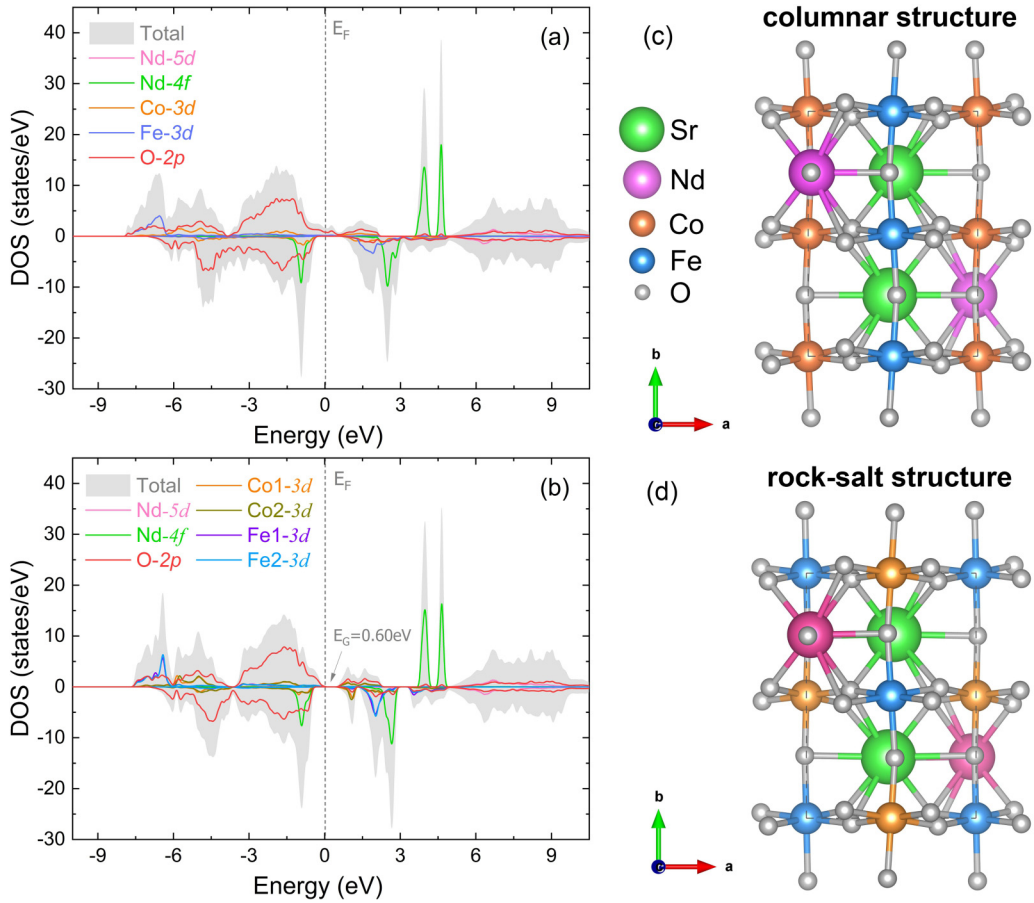

FIG. 11. (a) Total (TDOS) and (b) partial (PDOS) density of spin-polarized states of $NdSrCoFeO_6$ double perovskite alongside its corresponding (c) columnar and (d) rock-salt structures, as calculated by PBE + U method. The vertical dashed line indicates the Fermi energy level (E_F).

valence spin-up states crosses the Fermi energy, characterizing a metallic state. In contrast, the half-metallic nature of $NdSrCoFeO_6$ was indicated by the gap of ∼0.97 eV shown in the spin-down electronic bands, which is in agreement with values previously reported for other materials [124,125]. The PDOS at the valence band top is dominated by O $2p$ states hybridized with Co $3d$ orbitals and a narrow Nd $4f$ band in the spin-down channel. Moreover, an exchange splitting of the Co $3d$ electrons can be seen between −1.0 and −2.0 eV. The occupied Fe $3d$ states compose the spin-up valence band in lower-energy regions (∼−6.0 and −7.5 eV). The hybridization interaction of the oxygen $2p$ states is greater with Co $3d$ than with Fe $3d$ orbitals. This occurs because the higher magnetic moment on Fe sites favors exchange interactions that decrease the covalence of its chemical bonds with their neighboring ligands. The bottom composition of the conduction band is an admixture of Co and O states with a small, highlighted spin-down band of Fe ions. Empty Nd $4f$ states appear as a spin-down band nearing 2.0 eV and two more pronounced spin-up bands ∼4.5 eV. Further, unoccupied Nd $5d$ bands are located at higher-energy regions, between 6.0 and 9.0 eV, relative to the Fermi level. Similarly, we examine the spin-polarized DOS for the rock-salt system shown in Fig. 11(b). As can be seen, there is no significant change relative to the columnar cell. The electronic bands maintain practically the same shape, orbital character, and energy positions. In this new scenario, however, the Fermi level separates the valence band maximum and conduction band minimum in a well-defined manner by the energy bandgap of ∼0.60 eV. This is consistent with the experimental result shown in Fig. 7 for the resistivity behavior as a function of temperature. Furthermore, it also corroborates with the theoretical experimental results that de Oliveira *et al.* [13] report for Nd_2CoFeO_6, in which the authors conclude that the bandgap tends to increase as the magnetic moment at the Co site decreases. On the contrary, increasing the magnetic moment on Co implies increasing the metallic nature of the system. Herein, our calculations showed an interesting relationship between the number of disordered Fe/Co ions, their local magnetic moments, and the electronic nature of the sample, where increasing disorder leads to a decrease in the magnetic moment of Co, while the moment of Fe is increased, and there is a metal-semiconductor transition for the $NdSrCoFeO_6$.

Next, we further investigate the spin-state degree of the Fe and Co ions to better understand the microscopic inducing mechanism of AFM and FM in the $NdSrCoFeO_6$ system. To this end, we computed the magnetic t_{2g} (d_{xy}, d_{yz}, d_{zx}) and e_g (d_{z^2}, $d_{x^2-y^2}$) splitting of the $3d$ orbitals for the rock-salt structure.

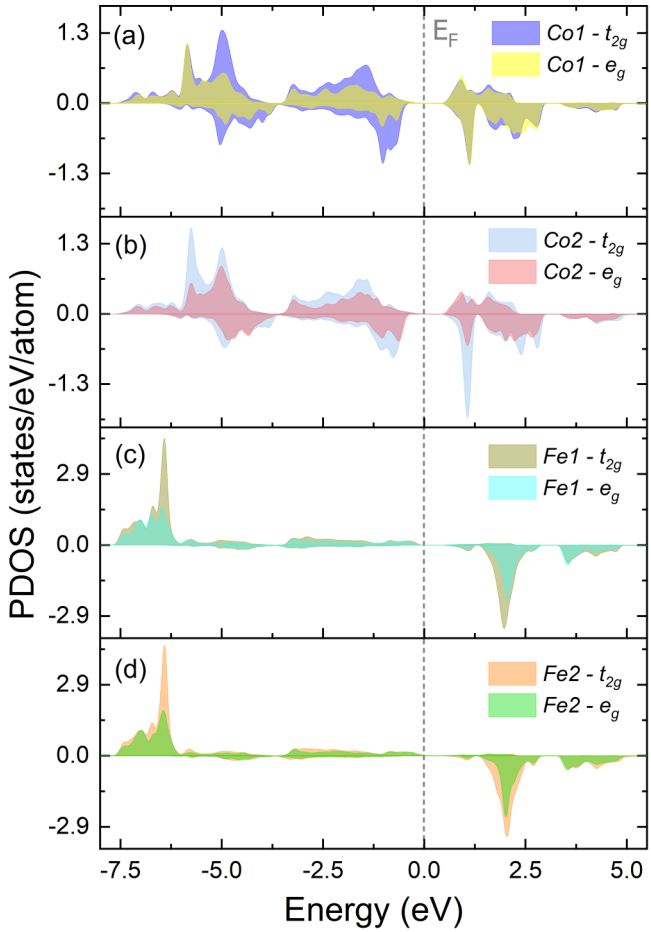

FIG. 12. Partial density of states (PDOS) up and down of (a) Co1 t_{2g} and Co1 e_g, (b) Co2 t_{2g} and Co2 e_g, (c) Fe1 t_{2g} and Fe1 e_g, and (d) Fe2 t_{2g} and Fe2 e_g. The vertical dashed line indicates the Fermi energy level (E_F).

Notably, we can see from the results shown in Fig. 12 that the electron occupancy of the Fe $3d$ spin-up and spin-down valence bands are four and one electrons, resulting in $3d^5$ (Fe^{3+}) with a $t_{2g}^3e_g^2$ HS state, respectively. For the Co $3d$ subshell, the orbital occupancy of four electrons in spin-up and two electrons in spin-down bands gives rise to the $3d^6$ (Co^{3+}) electronic configuration, suggesting the $3d^6$ orbital split in the $t_{2g}^5e_g^1$ intermediate-spin state or $t_{2g}^4e_g^2$ HS state (in agreement with our experimental predictions). We also analyzed the electron bands occupation of Co and Fe $3d$ orbitals in the columnar cell (see the Supplemental Material [123]), whereas significant similarities between the DOS shown in Figs. 11(a) and 11(b) are observed. The results for $3d^6$ (Co^{3+}) and $3d^5$ (Fe^{3+}) indicate that the effect of crystal field splitting on Co and Fe $3d$ orbitals produces equal spin states, as in the rock-salt structure. Additionally, our calculated DOS and PDOS showed a transition from semimetal (columnar structure) to semiconductor (rock-salt structure) nature. This electronic and observed magnetic behavior of the $NdSrCoFeO_6$ sample is a direct consequence of how the Co t_{2g} and e_g levels are occupied and how these states hybridize to the $2p$ states of its ligands. For the columnar structure, the octahedral intermediate-spin state of Co^{3+} consists of two unpaired electrons, one in e_g and the other within the t_{2g} orbital. The Co^{3+} e_g^1 electrons appear in the DOS as a band hybridized with the O $2p$ states that cross the Fermi level in the spin-up channel (see Figs. 11(a) and S2 in the Supplemental Material [123]) and characterize the $NdSrCoFeO_6$ with a semimetallic nature. When the rock-salt system is considered, the number of unpaired electrons in Co^{3+} $3d$ states increases to four, whereas two are in t_{2g} and the other two populate the e_g level, rising to the HS configuration. The higher number of unpaired electrons favors the hybridization significantly with the p states of neighboring oxygens [see Figs. 11(b) and 12]. Consequently, bonding and antibonding interactions are formed around the Fermi energy and give rise to the bandgap of $NdSrCoFeO_6$. Thus, changes in the electronic nature and magnetism of $NdSrCoFeO_6$ are a consequence of the spin-state transition from intermediate-spin Co^{3+} ($t_{2g}^5e_g^1$) to HS Co^{3+} ($t_{2g}^4e_g^2$) state.

Moreover, it is worth highlighting that the higher number of Fe ions in the rock-salt structure plays a key role in this process because it increases double exchange interactions with Co ions and decreases crystal field splitting between t_{2g} and e_g levels, favoring the transition from intermediate-spin to HS state. This explains the observed decrease in the local magnetic moment of Co and the increase of the local moment of the Fe ions for this structure. Accordingly, we inferred that the existence or predominance of each state (intermediate-spin or HS) depends on the Hund coupling energy, whereas the e_g state population increases by electron transfer whether the Hund coupling energy is close to the energy difference between the t_{2g} and e_g levels. This intermediate-spin state to HS state transition is favored by the combined effects of Co ion double exchange interaction increases and decreases in the crystal field splitting between t_{2g} and e_g levels due to the higher number of Fe ions in the rock-salt structure. Thereby, it is worth noting that the filling-induced spin-state transition from the HS state to the intermediate-spin state is also supported by the thermally driven metal-insulator transition for the $NdSrCoFeO_6$ sample, as shown in the temperature-dependent resistivity $\rho(T)$ curve (see Fig. 7).

As is well known, the magnetic outcome of linking two TM magnetic cations aleatorily distributed in the B sites of DP has been extensively discussed via electron localized models based on the Goodenough-Kanamori (G-K) rules, which assume that the dominant interactions are the crystal field splitting and in-plane superexchange interactions. Therefore, the G-K rules indicate that antiparallel spin coupling between the two nearest TM ions will have a strong tendency to align linearly, depending on the degree of octahedral tilt and distortion in this geometry. This superexchange 180° M-O-M′ (M,M′ = TMs) produces the major AFM spin interactions, whereas the MO_6 octahedra tilt in perovskite oxides reduces the bond angle so that a superexchange 90° M-O-M′ can generate strong FM couplings, but the tendency is much weaker than in the preceding case. However, there is still wide debate about these interactions splitting energy levels of $3d$ TMs in DPs. Additionally, the G-K rules are ambiguous for d^3-d^7 superexchange of magnetic ions distributed aleatorily in disordered B sites of DPs. Among several barely DP d^3-d^7 magnetic ions distributed in disordered B sites, Co-ion-based systems are fascinating because of Hund's rule

coupling (intersite interaction energy) as well as crystal-field interaction splitting Co $3d$ energy levels into narrow t_{2g} and e_g multiplets and also splitting the spin-up and spin-down states. On the other hand, our experimental results suggested that B and B′ sites of the Nd_2CoFeO_6 lattice are aleatorily occupied by $Co^{2+/3+}$ and $Fe^{3+/4+}$ ions, whereas an alternating distribution of $Co^{3+}O_6$ and $Fe^{3+}O_6$ octahedra throughout the lattice is predominant to keep the structure centrosymmetric. Since DPs containing magnetic ions at B sites are well known to be more sensitive to external environments, the ions interchanging positions, which is defined as ASD, play a key role in interrupting the long-range ordering of Co/Fe at B/B′ sites, while different microscopic electronic configurations between Co^{2+} with d^7 ($S = \frac{3}{2}$, $t_{2g}^6 e_g^1$ or $t_{2g}^5 e_g^2$) and Fe^{3+} with d^3 ($S = \frac{5}{2}$, $t_{2g}^4 e_g^1$) in the B/B′ sites contribute to reaching the electroneutrality of the $NdSrCoFeO_6$ structure by creating oxygen vacancies located at the AO_δ layers. Here, it is worth recalling that the sign of the transfer integral for 180° Co/Fe-O-Co/Fe superexchange interactions between octahedral-site cations is predicted to become AFM. Nevertheless, the somewhat high magnetic moment of $\sim 2.2\,\mu_B$, at measured 10 kOe at low temperature (2 K) experimentally found in the $NdSrCoFeO_6$ sample can only be explained in terms of (i) magnetization decreasing induced by stronger octahedral tilting in the AO_δ layers due to the accommodation of Sr^{2+} ions at A sites of the $NdSrCoFeO_6$ structure, (ii) spins canting effects in a low field, or (iii) ion pairs ferromagnetically coupled in the lattice induced by the ASD. Here, (i)–(iii) have failed as a picture to explain a magnetic moment as high as $2.2\,\mu_B$ measured in Sr/Co-based perovskites [126,127]. From this viewpoint, we argue that a hybridization-driven multisublattice double exchange and superexchange mechanism based on a localized electron picture cannot appropriately describe the microscopic origin of the inhomogeneous magnetic behavior of $NdSrCoFeO_6$ containing $Co^{2+/3+}$ and $Fe^{3+/4+}$ ions aleatorily occupying BB′ sites. Indeed, it seems evident that the somewhat high magnetic moment of $2.2\,\mu_B$ for our $NdSrCoFeO_6$ sample can be better explained by the itinerant-electron model proposed by Raccah and Goodenough [128]. In fact, our DFT calculations indicate that the presence of Fe favors oxygen-mediated double exchange interactions with Co ions, which leads to a decrease in the local magnetic moment of Co and, consequently, an increase in the local magnetic moment of Fe ions. Thus, it suggests that an itinerant state, which comes from the imbalance between the number of spin-up and spin-down conduction electrons in Co-Fe $3d$ ions, plays a significant role in the magnetism of $NdSrCoFeO_6$, even though there are contributions of the $4f$-Nd electrons. This dual electron itinerary and the localization characters have also been observed in $SrCoO_3$ and $La_{0.2}Sr_{0.8}CoO_{3-\delta}$ [127,129].

Lastly, it is widely known that chemical substitutions fine-tune FM double-exchange interactions mediated by chemically doped electron competition with the AFM superexchange interaction in perovskite-type materials. This means that a metal-insulator transition and a FM order develop according to carrier concentration-controlled competition. For our $NdSrCoFeO_6$ sample, the Fe^{3+}/Fe^{4+} and Co^{2+}/Co^{3+} ratio of ∼0.8–1.0 indicates that the magnitude and sign of the coupling are insensitive to the distance between magnetic ion pairs, and there obviously exists competition between localized and itinerant magnetism, as it has been previously reported for a perovskite compound [130]. Additionally, a spontaneous FM ordering smeared larger throughout ∼68 K up to the second transition temperature $T_{C2} = 149$ K (see Fig. 3) is observed, which is characteristic of itinerant-electron magnetism rather than of spin-spin interactions between localized-electron spins.

IV. CONCLUSIONS

We report a systematic study of the structural, magnetic, magnetocaloric properties, and critical behavior of the $NdSrCoFeO_6$ DP. Structural analysis showed that this sample crystallizes into a disordered orthorhombic (*Pnma*) structure at room temperature. The magnetization study showed the presence of multiple magnetic transitions at 20, 68, and 149 K, which are related to AFM canting order of the Co^{3+}/Fe^{3+} sublattice combined with PM behavior due to the Nd^{3+} ions; SG behavior due to ASD, which is associated with the presence of Fe^{4+} (LS), Fe^{3+}/Co^{2+} (HS), and Co^{3+} (HS/intermediate-spin); as well as a second-order magnetic transition from FM to PM state. The apparent GP behavior with $T_{GP} = 245$ K was confirmed by power law with exponent $\lambda = 0.74$. The MCE analysis reveals $-\Delta S_M^{max}$ and RCP of $1.84\,J\,kg^{-1}\,K^{-1}$ and $43.8\,J\,kg^{-1}$ at 40 kOe, respectively. The critical exponents were found to be $\beta = 1.384$, $\gamma = 0.621$, and $\delta = 1.421$, which are distant of any conventional universality class. DFT calculations reveal an interesting coupling between electronic and magnetic properties of the $NdSrCoFeO_6$ system. The observed changes in the magnetic moments of Co and Fe metal ions give rise to short- and long-range magnetic competitions of the material. The magnetic exchange distance $J(r)$ decreasing with $r^{-4.7}$, which in turn causes the negatively charged ligands to interact more strongly with the Co $3d$ orbitals and more weakly with the Fe $3d$ ones, should be responsible for the critical behavior. Analysis of the electronic bands showed that $NdSrCoFeO_6$ transitions from semimetallic to semiconducting, as illustrated by the bandgap of 0.6 eV. This transition, governed by complex hybridization between Co $3d$ and oxygen $2p$ states, is directly affected by the magnetic moment on the Co site.

ACKNOWLEDGMENTS

This paper was supported by the Coordenação de Aperfeiçoamento de Pessoal de Nível Superior-CAPES (Finance Code-001) and Conselho Nacional de Desenvolvimento Científico e Tecnológico-CNPq (Grants No. 309054/2019-2 and No. 309176/2019-0). Our thanks are also extended to the WIEN2K team of the Institute of Materials Chemistry (TU Vienna) and Multiuser Central Facilities (CEM-UFABC) for the WIEN2K code support and VSM facilities, respectively.

The authors declare no competing financial interest.

[1] A. Haque, R. Das, D. Ghosh, M. Vasundhara, A. Gayen, A. K. Kundu, and M. M. Seikh, J. Phys. Chem. C **125**, 3088 (2021).

[2] M. A. Pena and J. L. G. Fierro, Chem. Rev. **101**, 1981 (2001).

[3] K. Zhao, J. Chen, H. Li, A. Zheng, and F. He, J. Energy Inst. **92**, 594 (2019).

[4] S. U. Costilla-Aguilar, M. J. Escudero, R. F. Cienfuegos-Pelaes, and J. A. Aguilar-Martínez, J. Alloys Compd. **862**, 158025 (2021).

[5] S. Ben Hammouda, F. Zhao, Z. Safaei, D. L. Ramasamy, B. Doshi, and M. Sillanpää, Appl. Catal. B Environ. **233**, 99 (2018).

[6] H. Wu, X.-L. Shi, W.-D. Liu, M. Li, H. Gao, W. Zhou, Z. Shao, Y. Wang, Q. Liu, and Z.-G. Chen, Chem. Eng. J. **425**, 130668 (2021).

[7] P. Singh, M. Alam, S. Kumar, K. Anand, V. K. Gangwar, S. Ghosh, M. Sawada, K. Shimada, R. K. Singh, A. K. Ghosh *et al.*, J. Phys. Condens. Matter **32**, 445801 (2020).

[8] G. R. Haripriya, T. W. Heitmann, D. K. Yadav, G. C. Kaphle, M. P. Ghimire, R. Pradheesh, J. Joshi, P. Vora, K. Sethupathi, V. Sankaranarayanan *et al.*, J. Phys. Condens. Matter **33**, 025802 (2020).

[9] M. Balli, S. Jandl, P. Fournier, and A. Kedous-Lebouc, Appl. Phys. Rev. **4**, 021305 (2017).

[10] A. Pal, P. Singh, V. K. Gangwar, S. Ghosh, P. Prakash, S. K. Saha, A. Das, M. Kumar, A. K. Ghosh, and S. Chatterjee, Appl. Phys. Lett. **114**, 252403 (2019).

[11] R. C. Sahoo, Y. Takeuchi, A. Ohtomo, and Z. Hossain, Phys. Rev. B **100**, 214436 (2019).

[12] G. R. Haripriya, R. Pradheesh, M. N. Singh, A. K. Sinha, K. Sethupathi, and V. Sankaranarayanan, AIP Adv. **7**, 055826 (2017).

[13] L. S. de Oliveira, F. P. Sabino, D. Z. De Florio, A. Janotti, G. M. Dalpian, and J. A. Souza, J. Phys. Chem. C **124**, 22733 (2020).

[14] N. Das, S. Singh, A. G. Joshi, M. Thirumal, V. R. Reddy, L. C. Gupta, and A. K. Ganguli, Inorg. Chem. **56**, 12712 (2017).

[15] M. Das, P. Sarkar, and P. Mandal, Phys. Rev. B **101**, 144433 (2020).

[16] D. Mazumdar and I. Das, Phys. Chem. Chem. Phys. **23**, 5596 (2021).

[17] R. Pradheesh, H. S. Nair, C. M. N. Kumar, J. Lamsal, R. Nirmala, P. N. Santhosh, W. B. Yelon, S. K. Malik, V. Sankaranarayanan, and K. Sethupathi, J. Appl. Phys. **111**, 053905 (2012).

[18] A. Maignan, C. Martin, N. Nguyen, and B. Raveau, Solid State Sci. **3**, 57 (2001).

[19] A. Muñoz, J. A. Alonso, M. J. Martínez-Lope, C. de la Calle, and M. T. Fernández-Díaz, J. Solid State Chem. **179**, 3365 (2006).

[20] A. G. Silva, K. L. Salcedo Rodríguez, C. P. Contreras Medrano, G. S. G. Lourenco, M. Boldrin, E. Baggio-Saitovitch, and L. Bufaical, J. Phys. Condens. Matter **33**, 065804 (2020).

[21] M. Nasir, M. Khan, S. A. Agbo, S. Bhatt, S. Kumar, and S. Sen, J. Phys. D. Appl. Phys. **53**, 375003 (2020).

[22] H. G. Zhang, L. Xie, X. C. Liu, M. X. Xiong, L. L. Cao, and Y. T. Li, Phys. Chem. Chem. Phys. **19**, 25186 (2017).

[23] Z. Dong and S. Yin, Ceram. Int. **46**, 1099 (2020).

[24] X. Yang, J. Pan, S. Liu, M. Yang, L. Cao, D. Chu, and K. Sun, Phys. Rev. B **103**, 104405 (2021).

[25] D. N. Ba, Y. Zheng, L. Becerra, M. Marangolo, M. Almanza, and M. LoBue, Phys. Rev. Appl. **15**, 064045 (2021).

[26] Z. Yang, H. Zhang, M. Bai, W. Li, S. Huang, S. Ruan, and Y. J. Zeng, J. Mater. Chem. C **8**, 11866 (2020).

[27] K. Dey, A. Indra, S. Majumdar, and S. Giri, J. Mater. Chem. C **5**, 1646 (2017).

[28] R. C. Sahoo, S. Das, and T. K. Nath, J. Appl. Phys. **124**, 103901 (2018).

[29] J. Krishna Murthy, K. Devi Chandrasekhar, S. Mahana, D. Topwal, and A. Venimadhav, J. Phys. D. Appl. Phys. **48**, 355001 (2015).

[30] J. Rodríguez-Carvajal, Recent developments of the program fullprof, IUCr Newsletter **26**, 12 (2001); https://www.ill.eu/sites/fullprof/index.html

[31] M. Klinger and A. Jäger, J. Appl. Crystallogr. **48**, 2012 (2015).

[32] R. A. Brand, WINNORMOS Mössbauer Fitting Program, Universität Duisburg, 2008.

[33] P. Hohenberg and W. Kohn, Phys. Rev. **136**, B864 (1964).

[34] W. Kohn and L. J. Sham, Phys. Rev. **140**, A1133 (1965).

[35] O. K. Andersen, Phys. Rev. B **12**, 3060 (1975).

[36] P. Blaha, K. Schwarz, G. K. H. Madsen, D. Kvasnicka, J. Luitz, R. Laskowski, F. Tran, and L. D. Marks, *WIEN2K, An Augmented Plane Wave + Local Orbitals Program for Calculating Crystal Properties* (Vienna University of Technology, Vienna, 2018).

[37] J. P. Perdew, A. Ruzsinszky, G. I. Csonka, O. A. Vydrov, G. E. Scuseria, L. A. Constantin, X. Zhou, and K. Burke, Phys. Rev. Lett. **100**, 136406 (2008).

[38] V. I. Anisimov, A. I. Poteryaev, M. A. Korotin, A. O. Anokhin, and G. Kotliar, J. Phys. Condens. Matter **9**, 7359 (1997).

[39] S. N. Qadri, S. B. Qadri, D. H. Wu, R. Goswami, and M. Osofsky, AIP Adv. **8**, 105316 (2018).

[40] J.-H. Kim, F. Prado, and A. Manthiram, J. Electrochem. Soc. **155**, B1023 (2008).

[41] K. Momma and F. Izumi, J. Appl. Crystallogr. **41**, 653 (2008).

[42] R. R. Das, P. N. Lekshmi, S. C. Das, and P. N. Santhosh, J. Alloys Compd. **773**, 770 (2019).

[43] R. D. Shannon, Acta Crystallogr. Sect. A **32**, 751 (1976).

[44] S. M. Borchani, W. C. R. Koubaa, and M. Megdiche, R. Soc. Open Sci. **4**, 170920 (2017).

[45] M. T. Anderson, K. B. Greenwood, G. A. Taylor, and K. R. Poeppelmeier, Prog. Solid State Chem. **22**, 197 (1993).

[46] K. Aswathi, J. P. Palakkal, P. N. Lekshmi, and M. R. Varma, New J. Chem. **43**, 17351 (2019).

[47] T. K. Mandal and J. Gopalakrishnan, Chem. Mater. **17**, 2310 (2005).

[48] A. Muñoz, J. A. Alonso, M. T. Casais, M. J. Martínez-Lope, and M. T. Fernández-Díaz, J. Phys. Condens. Matter **14**, 3285 (2002).

[49] S. Zhao, L. Gao, C. Lan, S. S. Pandey, S. Hayase, and T. Ma, RSC Adv. **6**, 43034 (2016).

[50] J. H. Kim and A. Manthiram, J. Mat. Chem. A **3**, 24195 (2015).

[51] G. Zhang, H. Chen, Z. Gu, P. Zhang, T. Zeng, and F. Huang, Inorg. Chem. **56**, 10404 (2017).

[52] J. P. Bolletta, F. Pomiro, R. D. Sánchez, V. Pomjakushin, G. Aurelio, A. Maignan, C. Martin, and R. E. Carbonio, Phys. Rev. B **98**, 134417 (2018).

[53] R. Pradheesh, H. S. Nair, G. R. Haripriya, A. Senyshyn, T. Chatterji, V. Sankaranarayanan, and K. Sethupathi, J. Phys. Condens. Matter **29**, 095801 (2017).

[54] W. K. Zhu, C. K. Lu, W. Tong, J. M. Wang, H. D. Zhou, and S. X. Zhang, Phys. Rev. B **91**, 144408 (2015).

[55] L. Zhang, T. L. Shi, J. J. Cao, S. M. Yan, Y. Fang, Z. D. Han, B. Qian, X. F. Jiang, and D. H. Wang, J. Alloys Compd. **763**, 613 (2018).

[56] D. Yang, T. Yang, P. Mukherjee, S. E. Dutton, D. Huo, and M. A. Carpenter, Phys. Rev. B **99**, 094314 (2019).

[57] R. C. Sahoo, S. K. Giri, D. Paladhi, A. Das, and T. K. Nath, J. Appl. Phys. **120**, 033906 (2016).

[58] J. Y. Moon, M. K. Kim, D. G. Oh, J. H. Kim, H. J. Shin, Y. J. Choi, and N. Lee, Phys. Rev. B **98**, 174424 (2018).

[59] J. Krishna Murthy, K. D. Chandrasekhar, H. C. Wu, H. D. Yang, J. Y. Lin, and A. Venimadhav, J. Phys. Condens. Matter **28**, 086003 (2016).

[60] S. K. Upadhyay, K. K. Iyer, S. Rayaprol, V. Siruguri, and E. V. Sampathkumaran, J. Mater. Chem. C **5**, 5163 (2017).

[61] P. N. Lekshmi, G. R. Raji, M. Vasundhara, M. R. Varma, S. S. Pillai, and M. Valant, J. Mater. Chem. C **1**, 6565 (2013).

[62] J. Liu, J. Luo, Q. Han, J. Cao, L. Chen, Y. Song, and L. Chen, J. Mater. Chem. C **5**, 2043 (2017).

[63] P. A. Kumar, R. Mathieu, P. Nordblad, S. Ray, O. Karis, G. Andersson, and D. D. Sarma, Phys. Rev. X **4**, 011037 (2014).

[64] S. Lin, D. F. Shao, J. C. Lin, L. Zu, X. C. Kan, B. S. Wang, Y. N. Huang, W. H. Song, W. J. Lu, P. Tong *et al.*, J. Mater. Chem. C **3**, 5683 (2015).

[65] J. P. Palakkal, C. Raj Sankar, and M. R. Varma, J. Appl. Phys. **122**, 073907 (2017).

[66] S. Pal, S. Jana, S. Govinda, B. Pal, S. Mukherjee, S. Keshavarz, D. Thonig, Y. Kvashnin, M. Pereiro, R. Mathieu *et al.*, Phys. Rev. B **100**, 045122 (2019).

[67] I. Fita, I. O. Troyanchuk, T. Zajarniuk, P. Iwanowski, A. Wisniewski, and R. Puzniak, Phys. Rev. B **98**, 214445 (2018).

[68] D. Bhoi, N. Khan, A. Midya, M. Nandi, A. Hassen, P. Choudhury, and P. Mandal, J. Phys. Chem. C **117**, 16658 (2013).

[69] A. Pal, P. Singh, V. K. Gangwar, A. G. Joshi, P. Khuntia, G. D. Dwivedi, P. K. Gupta, M. Alam, K. Anand, K. Sethupathi *et al.*, J. Phys. Condens. Matter **32**, 215801 (2020).

[70] W. Liu, L. Shi, S. Zhou, J. Zhao, Y. Li, and Y. Guo, J. Appl. Phys. **116**, 193901 (2014).

[71] Y. R. Uhm, S. J. Kim, and C. S. Kim, J. Magn. **7**, 18 (2002).

[72] T. C. Gibb, J. Mater. Chem. **2**, 415 (1992).

[73] R. Pradheesh, H. S. Nair, V. Sankaranarayanan, and K. Sethupathi, Eur. Phys. J. B **85**, 260 (2012).

[74] T. R. Cummins and R. G. Egdell, Phys. Rev. B **48**, 6556 (1993).

[75] S. Raaen and R. D. Parks, J. Magn. Magn. Mater. **47–48**, 200 (1985).

[76] K. Tanwar, D. S. Gyan, S. Bhattacharya, S. Vitta, A. Dwivedi, and T. Maiti, Phys. Rev. B **99**, 174105 (2019).

[77] K. F. Hsu, C. L. Wu, S. C. Huang, C. M. Wu, J. R. Hsiao, Y. T. Yo, Y. H. Chen, A. L. Shiau, and C. Y. Chou, Autophagy **5**, 451 (2009).

[78] J. Haber and L. Ungier, J. Electron Spectros. Relat. Phenomena **12**, 305 (1977).

[79] B. Liu, Y. Zhang, and L. Tang, Int. J. Hydrogen Energy **34**, 435 (2009).

[80] J. Kuyyalil, D. Newby, J. Laverock, Y. Yu, D. Cetin, S. N. Basu, K. Ludwig, and K. E. Smith, Surf. Sci. **642**, 33 (2015).

[81] J. Santiso, J. Fraxedas, and A. Figueras, Surf. Sci. Spectra **9**, 39 (2002).

[82] J. Santiso, J. Fraxedas, L. Balcells, J. Fontcuberta, and A. Figueras, J. Phys. IV France **11**, Pr11-307 (2001).

[83] R. S. Silva Jr., N. S. Ferreira, J. F. D. Fontes, M. E. H. Maia da Costa, and P. Barrozo, Chem. Phys. Lett. **787**, 139278 (2022).

[84] N. A. Merino, B. P. Barbero, P. Eloy, and L. E. Cadús, Appl. Surf. Sci. **253**, 1489 (2006).

[85] A. K. Opitz, C. Rameshan, M. Kubicek, G. M. Rupp, A. Nenning, T. Götsch, R. Blume, M. Hävecker, A. Knop-Gericke, G. Rupprechter *et al.*, Top. Catal. **61**, 2129 (2018).

[86] P. A. W. Van Der Heide, Surf. Interface Anal. **33**, 414 (2002).

[87] A. Yan, V. Maragou, A. Arico, M. Cheng, and P. Tsiakaras, Appl. Catal. B Environ. **76**, 320 (2007).

[88] E. K. Abdel-Khalek, M. A. Motawea, M. A. Aboelnasr, and H. H. El-Bahnasawy, Phys. B Condens. Matter **624**, 413415 (2022).

[89] X. M. Xu, L. Shi, S. Y. Pan, J. Y. Zhao, and R. X. Tong, J. Appl. Phys. **129**, 175301 (2021).

[90] R. Guan, Z. Wang, H. Xu, X. Hao, L. Yang, J. Liu, S. Yu, and T. He, ACS Appl. Energy Mater. **5**, 481 (2022).

[91] C. Zobel, M. Kriener, D. Bruns, J. Baier, M. Grüninger, T. Lorenz, P. Reutler, and A. Revcolevschi, Phys. Rev. B **66**, 020402(R) (2002).

[92] M. A. Korotin, S. Yu. Ezhov, I. V. Solovyev, V. I. Anisimov, D. I. Khomskii, and G. A. Sawatzky, Phys. Rev. B **54**, 5309 (1996).

[93] J. Kanamori, J. Phys. Chem. Solids **10**, 87 (1959).

[94] S. Pal, S. Govinda, M. Goyal, S. Mukherjee, B. Pal, R. Saha, A. Sundaresan, S. Jana, O. Karis, J. W. Freeland, and D. D. Sarma, Phys. Rev. B **97**, 165137 (2018).

[95] J. P. Palakkal, C. R. Sankar, A. P. Paulose, and M. R. Varma, J. Alloys Compd. **743**, 403 (2018).

[96] S. Kivelson, Phys. Rev. B **25**, 3798 (1982).

[97] A. Arrott and J. E. Noakes, Phys. Rev. Lett. **19**, 786 (1967).

[98] A. Arrott, Phys. Rev. **108**, 1394 (1957).

[99] J. Y. Law, V. Franco, L. M. Moreno-Ramírez, A. Conde, D. Y. Karpenkov, I. Radulov, K. P. Skokov, and O. Gutfleisch, Nat. Commun. **9**, 2680 (2018).

[100] D. Mazumdar and I. Das, J. Appl. Phys. **129**, 063901 (2021).

[101] V. Franco, J. S. Blázquez, J. J. Ipus, J. Y. Law, L. M. Moreno-Ramírez, and A. Conde, Prog. Mater. Sci. **93**, 112 (2018).

[102] V. Franco, J. S. Blázquez, and A. Conde, Appl. Phys. Lett. **89**, 222512 (2006).

[103] R. Das, A. Midya, M. Kumari, A. Chaudhuri, X. Yu, A. Rusydi, and R. Mahendiran, J. Phys. Chem. C **123**, 3750 (2019).

[104] S. Tillaoui, A. El Boubekri, A. Essoumhi, M. Sajieddine, E. K. Hlil, R. Moubah, M. Sahlaoui, A. Razouk, and H. Lassri, Mater. Sci. Eng. B **266**, 115052 (2021).

[105] S. Mondal, A. Midya, M. M. Patidar, V. Ganesan, and P. Mandal, Appl. Phys. Lett. **117**, 092405 (2020).

[106] J. Krishnamurthy and A. Venimadhav, J. Magn. Magn. Mater. **500**, 166387 (2020).

[107] Y. Jia, Y. Cheng, H. Wang, Z. Zhang, and L. Li, Ceram. Int. **46**, 25043 (2020).

[108] C. L. Li, L. G. Wang, X. X. Li, C. M. Zhu, R. Zhang, H. W. Wang, and S. L. Yuan, Mater. Chem. Phys. **202**, 76 (2017).

[109] Y. Zhang, H. Li, D. Guo, L. Hou, X. Li, Z. Ren, and G. Wilde, Ceram. Int. **44**, 20762 (2018).
[110] L. Li, P. Xu, S. Ye, Y. Li, G. Liu, D. Huo, and M. Yan, Acta Mater. **194**, 354 (2020).
[111] B. Wu, D. Guo, Y. Wang, and Y. Zhang, Ceram. Int. **46**, 11988 (2020).
[112] N. Khan, A. Midya, K. Mydeen, P. Mandal, A. Loidl, and D. Prabhakaran, Phys. Rev. B **82**, 064422 (2010).
[113] L. Zhang, D. Menzel, C. Jin, H. Du, M. Ge, C. Zhang, L. Pi, M. Tian, and Y. Zhang, Phys. Rev. B **91**, 024403 (2015).
[114] A. K. Pramanik and A. Banerjee, Phys. Rev. B **79**, 214426 (2009).
[115] Y. Liu and C. Petrovic, Phys. Rev. B **97**, 014420 (2018).
[116] L. Su, X. Q. Zhang, Q. Y. Dong, Y. J. Ke, K. Y. Hou, C. S. Liu, and Z. H. Cheng, J. Alloys Compd. **746**, 594 (2018).
[117] M. Jeddi, J. Massoudi, H. Gharsallah, S. I. Ahmed, E. Dhahri, and E. K. Hlil, RSC Adv. **11**, 7238 (2021).
[118] Y. Li, Q. Lv, S. Feng, K. M. Ur Rehman, X. Kan, and X. Liu, Ceram. Int. **47**, 32599 (2021).
[119] H. Yanagihara, W. Cheong, M. B. Salamon, S. Xu, and Y. Moritomo, Phys. Rev. B **65**, 092411 (2002).
[120] R. P. Madhogaria, R. Das, E. M. Clements, V. Kalappattil, M. H. Phan, H. Srikanth, N. T. Dang, D. P. Kozlenko, and N. S. Bingham, Phys. Rev. B **99**, 104436 (2019).
[121] K. Ghosh, C. J. Lobb, R. L. Greene, S. G. Karabashev, D. A. Shulyatev, A. A. Arsenov, and Y. Mukovskii, Phys. Rev. Lett. **81**, 4740 (1998).
[122] A. Rahman, M. U. Rehman, D. Zhang, M. Zhang, X. Wang, R. Dai, Z. Wang, X. Tao, L. Zhang, and Z. Zhang, Phys. Rev. B **100**, 214419 (2019).
[123] See Supplemental Material at http://link.aps.org/supplemental/10.1103/PhysRevB.106.134439 for an overview of data tables showing the structural parameters and vesta images of all simulated configurations.
[124] H. Wu, L. Wang, Y. Qian, W. Tan, C. Xiao, and K. Deng, J. Appl. Phys. **110**, 083701 (2011).
[125] K. Samanta, P. Sanyal, and T. Saha-Dasgupta, Sci. Rep. **5**, 15010 (2015).
[126] S. Medling, Y. Lee, H. Zheng, J. F. Mitchell, J. W. Freeland, B. N. Harmon, and F. Bridges, Phys. Rev. Lett. **109**, 157204 (2012).
[127] M. Chennabasappa, E. Petit, and O. Toulemonde, Ceram. Int. **46**, 6067 (2020).
[128] P. M. Raccah and J. B. Goodenough, J. Appl. Phys. **39**, 1209 (1968).
[129] V. Pralong, V. Caignaert, S. Hébert, C. Marinescu, B. Raveau, and A. Maignan, Solid State Ion. **177**, 815 (2006).
[130] J. T. Mefford, X. Rong, A. M. Abakumov, W. G. Hardin, S. Dai, A. M. Kolpak, K. P. Johnston, and K. J. Stevenson, Nat. Commun. **7**, 11053 (2016).